THE MICHIGAN STATE UNIVERSITY SUPERCONDUCTING CYCLOTRON PROGRAM*

Lab Staff

Summary

Status of the superconducting cyclotron program is reviewed as of September 1978. A number of design details have changed since the previous conference. Novel features have been checked in a variety of prototype test facilities.

Text

In June 1975 the MSU Cyclotron Laboratory received authorization to proceed with construction of a full scale prototype magnet for a 500 MeV superconducting cyclotron. The objective of this program was to establish basic feasibility of accelerator systems using such magnets. In May 1977 operating tests of the prototype magnet were started; first operation at full design current occurred on May 26, 1977. Overall performance of the prototype magnet was excellent and in August 1977 the laboratory received authorization to proceed with a so called "Phase I" accelerator program, namely, a program to make the 500 MeV magnet into a working cyclotron and to connect this cyclotron with existing experimental facilities. This Phase I program is very much in mid-stream at present. First operating tests of the cyclotron are expected in the Fall of 1979 and nuclear physics use is expected to begin early in 1980. The laboratory has also submitted a proposal for a further major expansion, namely adding a second 800 MeV superconducting cyclotron as a booster for the 500 MeV machine and including additions to the laboratory building and to experimental facilities which would approximately double the size of the present installation. The proposal has received a high priority recommendation for funding in fiscal year 1980. If this proceeds as planned the full two cyclotron system is expected to come into use in early 1984.

Many of the subsystems of this overall project are described in specific topical papers appearing elsewhere in these proceedings i.e., central region, rf system, cryogenic system, magnetic field studies, trimming optimization studies, extraction studies, injection studies for the second stage, and overall design of the K800 cyclotron. The objective of this summary paper is to convey a somewhat more casual and largely pictorial glimpse of the actual status of the project as of September, 1978.

The core of the presentation is in the following six pages which present Figures 1 through 23. These figures and the technical comments included with the captions show a number of construction details of the K500 cyclotron and performance expected from the system. The figures also show a number of prototype assemblies built to test various features of the design.

In reviewing the figures, a number of major design changes can be seen relative to descriptions given at the 1975 cyclotron conference reflecting evolution of design concepts as the program evolved as well as adaptations to unexpected results from some protopype tests. The idea of using an inert superconducting extraction channel has been laid aside, for example following a series of prototype tests of these so called "super-tubes", which gave a mixture of good and bad results and a sense of inadequate reliability of such elements as a key subsystem of a major accelerator project. The presently envisaged extraction system then consists of electrostatic deflectors which operate well within established technical limits on electric fields. The electrostatic deflectors are supplemented by sets of inert iron focusing bars positioned in a pattern which gives a field combining a strong quadrupole and a weak dipole component. The overall combination of deflector and focusing bars gives a very attractive extraction trajectory with excellent optical characteristics.

A major change in the rf system relative to the 1975 design is a lowering of the frequency range by an approximate factor of 3 and a correlated decision to make extensive use of harmonic numbers 1, 2, 4, etc., which require phasing of the dees by multiples of 120°. Phasing of 120° is a feature not previously used in cyclotrons except for a brief early test at Berkeley and a rather realistic model was therefore built to check tuning characteristics of a system of this kind. Orbit properties of the overall system are much improved by having the rf frequency more nearly match the orbital frequency and an overall sizeable improvement in beam quality is expected from the lower frequency system.

The lower frequency range involves dee stems of rather awkward length--at 9 Mhz the sliding short is $\sim$ 16' from the median plane--estimates of mechanical vibrations in dee stems of this length indicated serious problems for 4" diameter unsupported stems. Dee stem insulators have therefore been introduced just below the magnet yoke. These also then form a boundary for the vacuum envelope and allow the sliding shorts which tune the dees to operate in air.

The vacuum system for the cyclotron is a somewhat complicated three part chamber, namely a completely separate all metal enclosure as the insulating jacket for the main coil, secondly, a high quality cryopumped metal gasketed chamber for the beam space and thirdly, a low quality "coil" vacuum contained between the pole caps and the copper rf liners enclosing both pole tips and pole tip correction windings.

*Work supported by the U.S. National Science Foundation Grant #s 75-01080, PHY76-83254, and PHY78-01684.

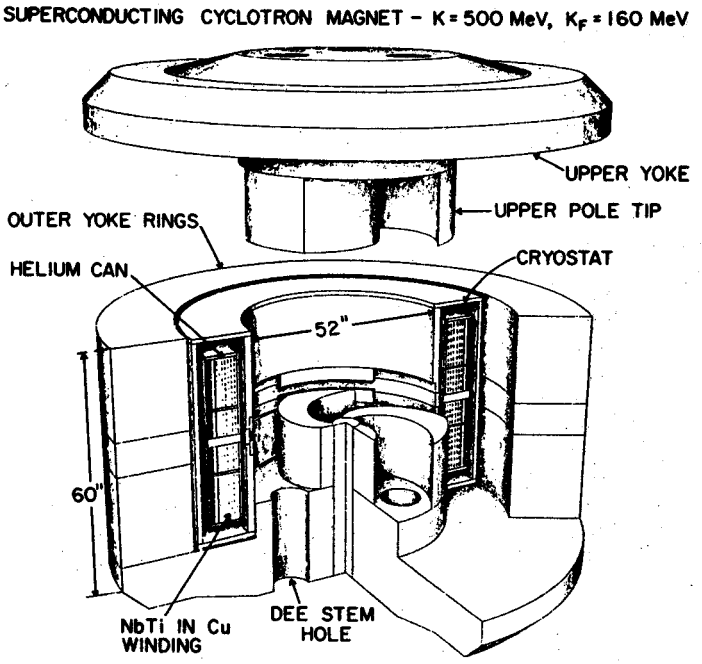

Figure 1. Conceptual drawing of the K500 magnet showing major elements of the coil, yoke, and pole tip system. The upper pole cap is in the raised position. The cryostat wall is constructed of mild steel except for a non-magnetic median plane insert.

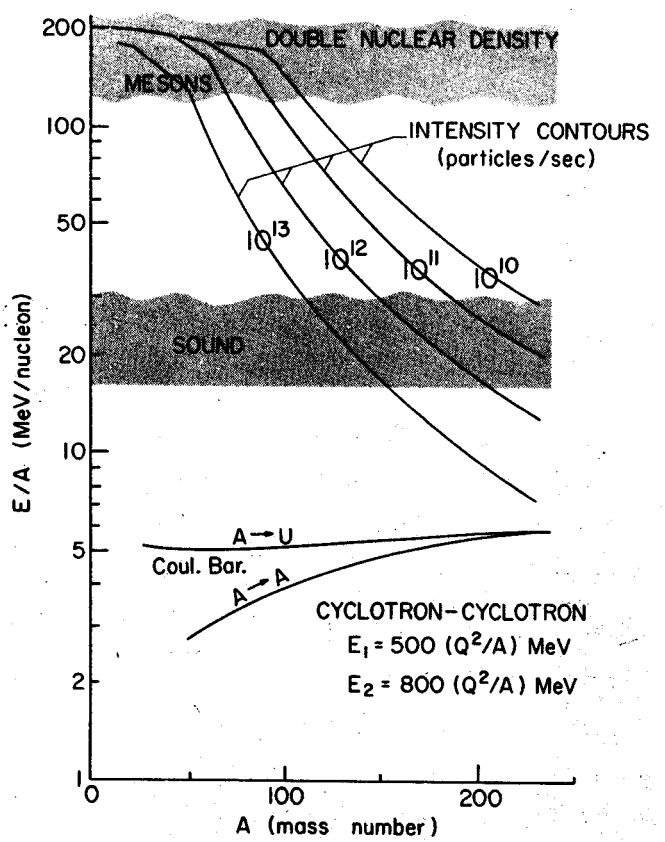

Figure 2. Approximate smoothed intensity contours for coupled K500 and K800 cyclotrons. The gray bands show the overlap between the operating range and theoretical estimates of the onset of nuclear compressional waves, coherent mesic phenomena and doubling of the nuclear density. (More accurate performance estimates based on detailed calculation of the K800 are given in the paper by Resmini.)

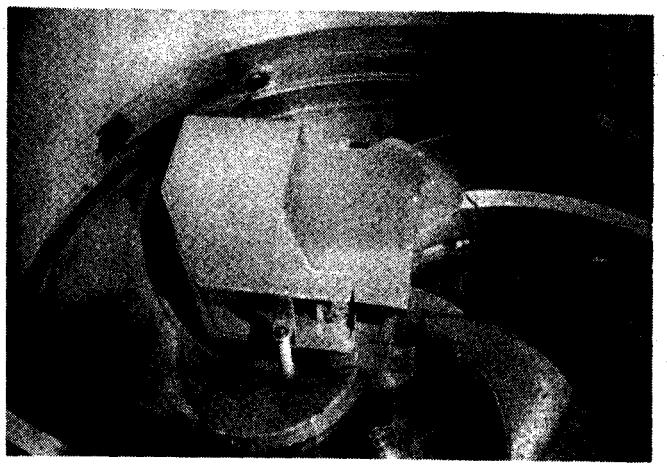

Figure 3. Photograph of lower pole tip with ion source testing charge collector mounted in position. (The charge collector operates at DC bias of 30 kV and is equipped with a multi-wire collecting grid for study of charge state distributions.)

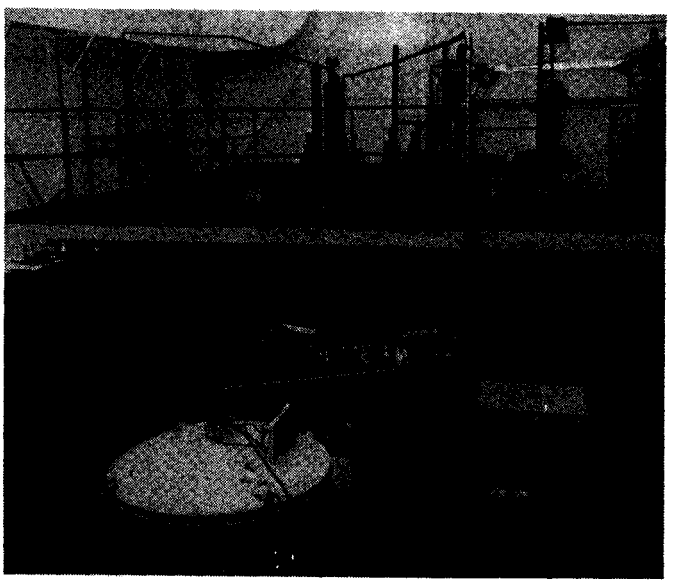

Figure 4. View of the helium refrigerator and liquid storage tank with the K500 magnet in the background.

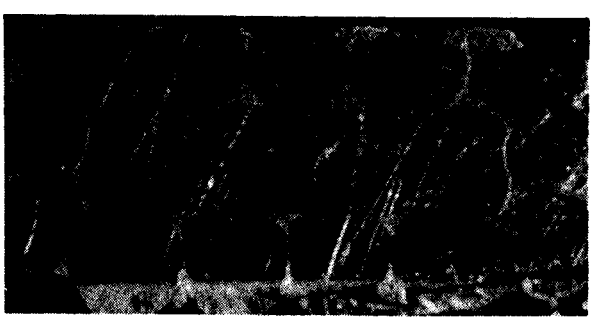

Figure 5. Conductor magnified 15x. Niobium-titanium filaments are embedded in three 40 mil diameter copper wires located at the left and at the upper and lower right in the photo. (Each bundle contains 115 filaments, each 2 mils in diameter.) The three superconducting bundles are spirally wrapped along with ten pure copper wires around a rectangular copper core and bonded with soft solder to form an overall 0.110" by 0.196" conductor.

Figure 6. (right) Vertical section view of the K500 cyclotron. (In the pole tip region the section view is along a line of constant spiral.) The coil is held in position by a set of nine support links (3 up, 3 down, 3 radial) constructed of epoxy and fiber-glass laminate. The lower half of each dee contains a cryo-panel which directly views the beam space. The rf drive line feeds through a cup shaped variable capacitor which can be seen at the outer edge of the lower part of the dee. Identical non-magnetic ion sources enter from top and bottom vacuum locks at the cyclotron center, so that cathode changes and source pump-out can be performed while the cyclotron is running on the other source.

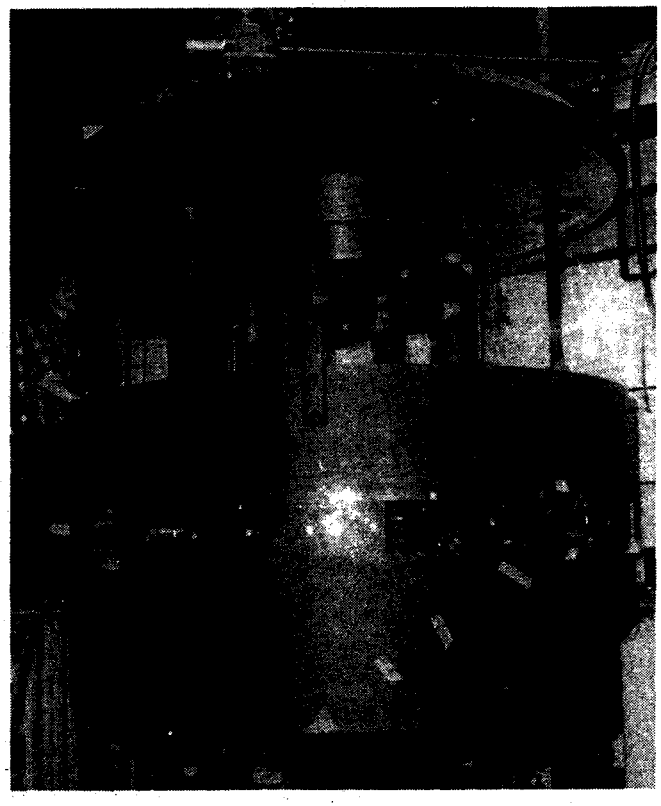

Figure 7. Photograph of the K500 magnet with top raised for access. The upper set of pole tips can be seen near the center.

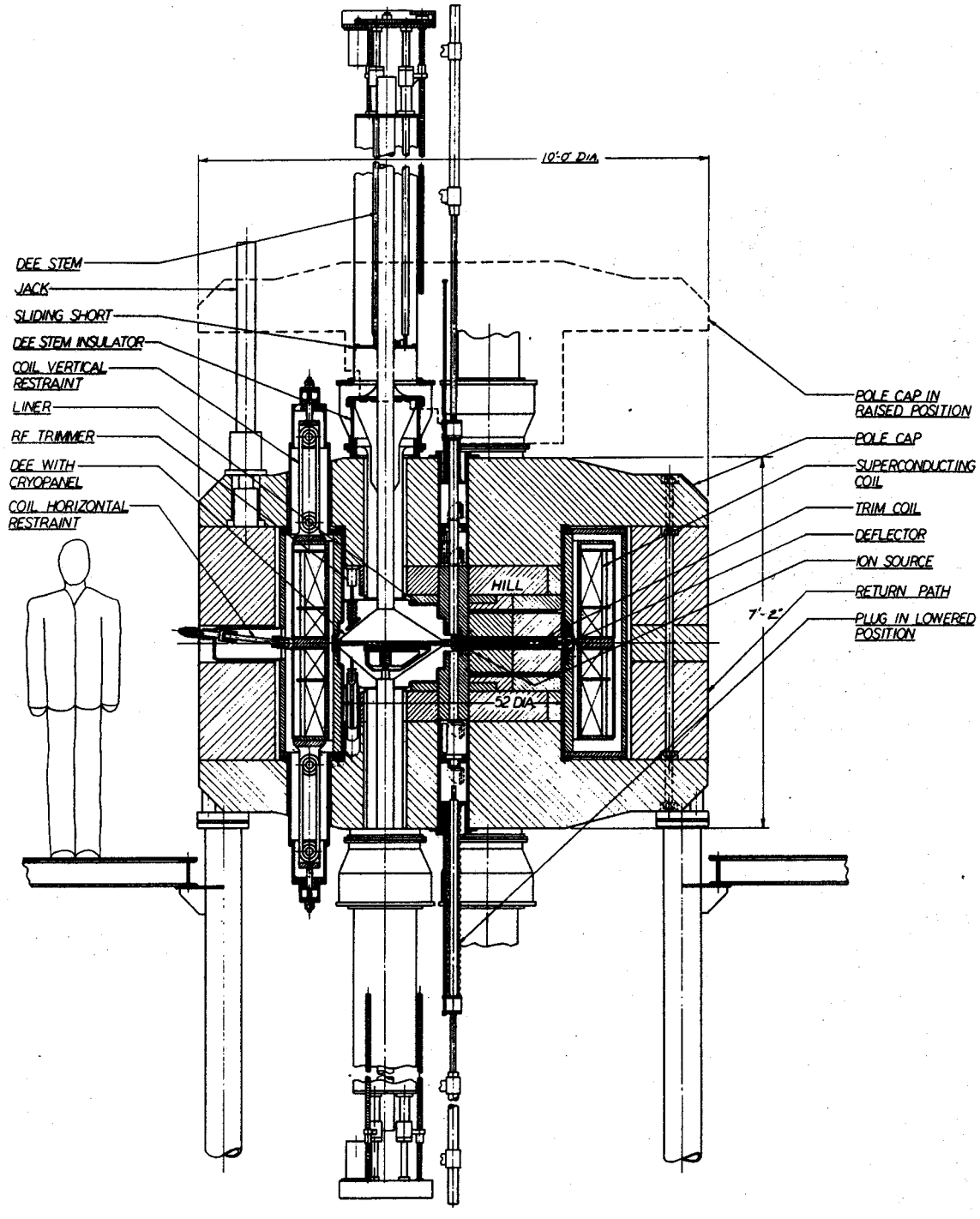

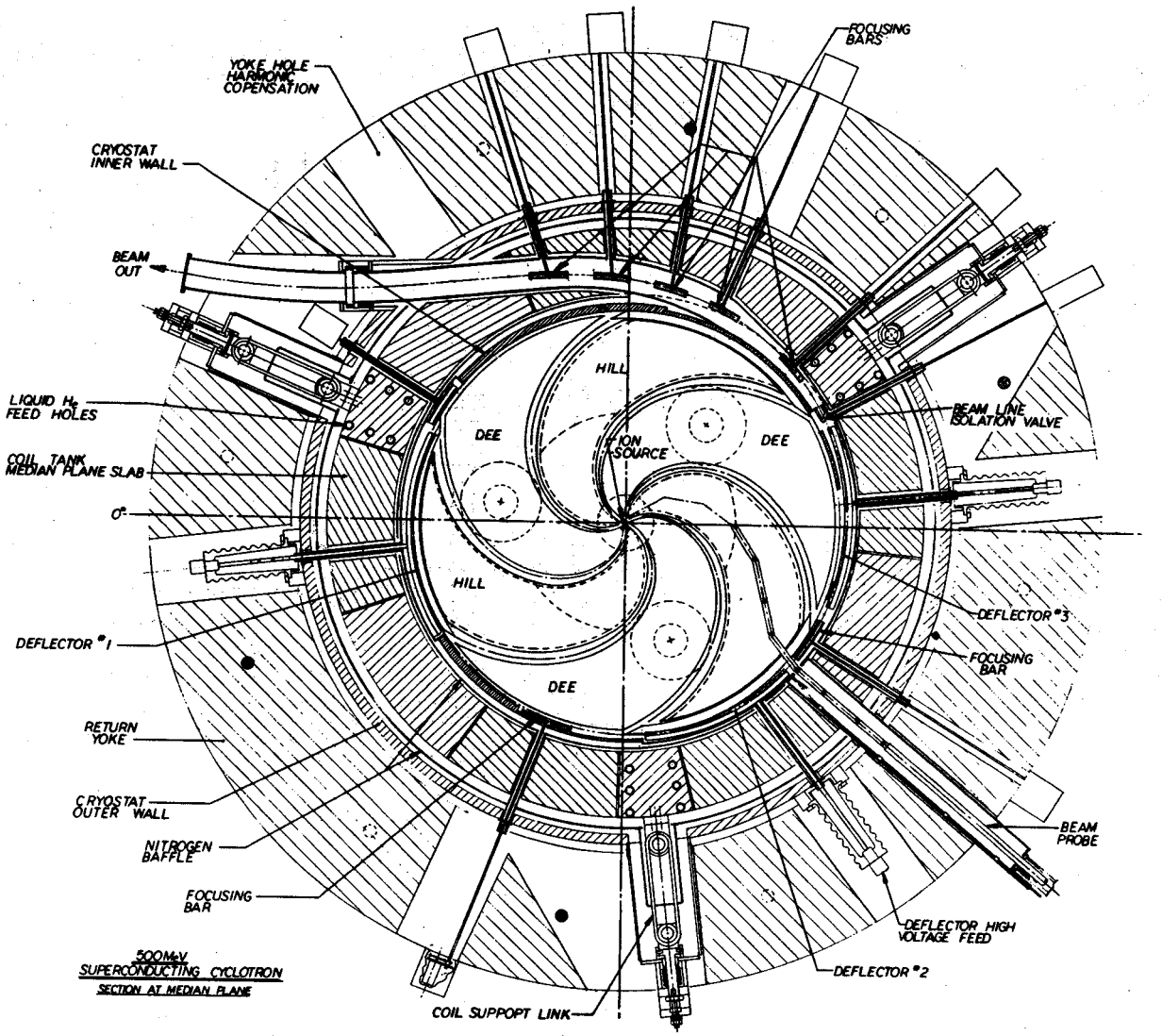

Figure 8. Median plane view of the K500 cyclotron. Dashed lines mark the edge of the pole tip steel and the dee stem and dee stem housing. The dot-dashed lines show the design angular location of the acccelerating gaps ($\tau = r/13" + n\times\pi/3$). The helium bath for the upper and lower sections of the main coil connects only through the 18 "liquid helium feed holes." The remainder of the median plane periphery of the coil is composed of stainless steel slabs which can be removed for installation of median plane penetrations (extraction elements, probes, etc.).

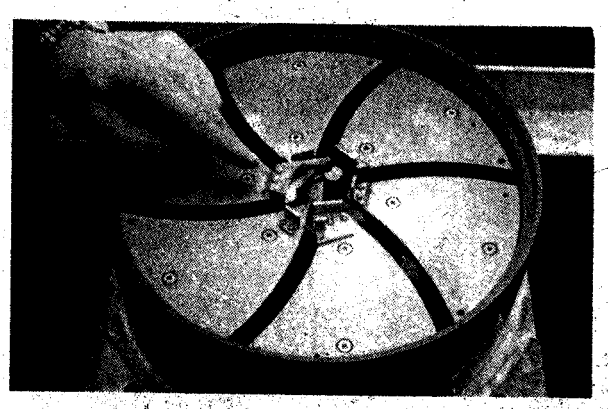

Figure 9. Photo of three dimensional one-to-one scale electrolyte tank. The lip of the tank wall (and the surface of the central electrodes) marks the median plane. The source position and other central region structures are set for first harmonic operation.

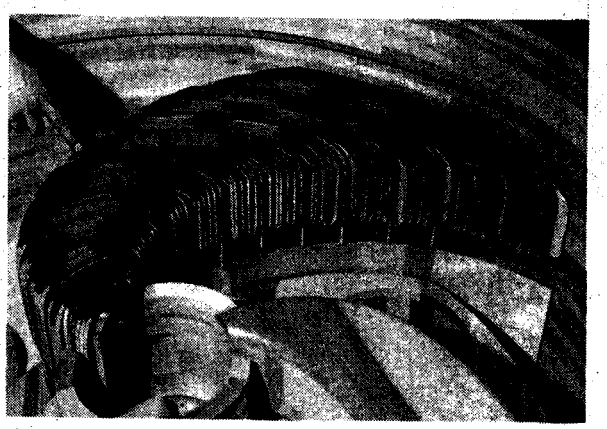

Figure 10. Prototype set of trim coils mounted on the full scale wooden model. The dark line on the outer periphery marks the median plane. Each of the thirteen coils has nine and one half turns of 0.25" x 0.25" hollow copper conductor.

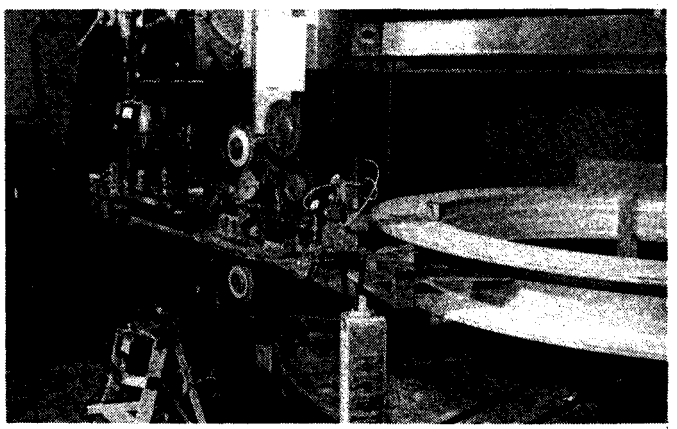

Figure 11. Photograph of the coil winding machine set up for practice winding. Mylar insulation (stored on the circular reels) was creased and applied to the conductor directly in the winding line in a fashion which left the conductor surface 50% bare. The winding line also includes an accurate tensioning system (with the capability of maintaining tensioning during possible unwinding cycles), a presser foot to pack each turn of conductor tightly against its neighbor, a dimension checking circuit to monitor the conductor for possible protruding filaments and a feed mechanism which advances the whole winding apparatus helically along the coil.

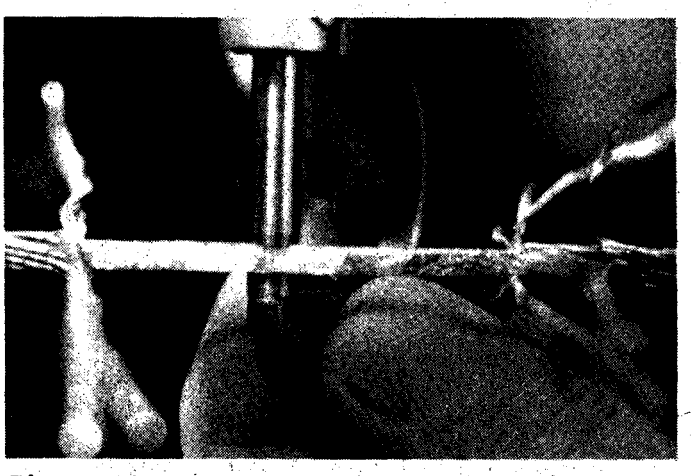

Figure 12. Photograph of conductor in the process of splicing. The central copper core has been joined in a scarf type hard solder joint. The conductor filaments will next be rebraided in rope-like fashion and soft soldered (13 of the copper strands being clipped at staggered points). The coil contains 15 such splices. Acceptable splices did not exceed the linear dimension of the unspliced conductor by more than 10 mils. A resistance measurement on a test splice gave 1.4×10^{-9} ohms at 4.2° and 5 tesla. Pull tests on 5 samples gave values greater than 90% of the breaking strength of unspliced conductor.

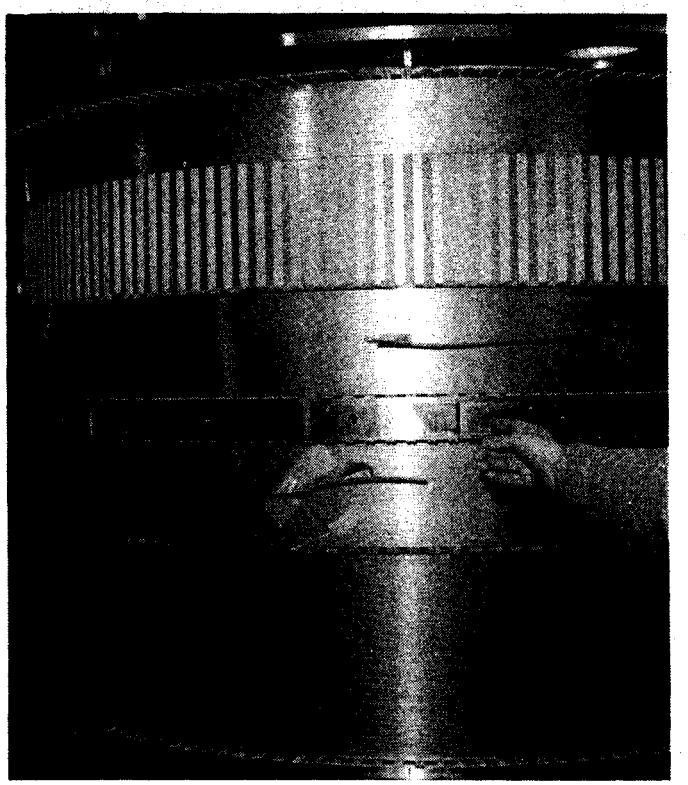

Figure 13. Photograph of the coil near the end of the winding cycle. The hand touches one of the removable stainless steel median plane slabs. Winding of the two small coil sections near the median plane and of the lower large section is completed, and winding of the upper large coil section is nearing completion. The vertical "picket fence" across the upper center is a layer of 40 mil thick G-10 strips inserted between conductor layers, the regions between the strips forming channels for liquid helium. At the point when the photograph was taken, a coil layer is approximately 30% finished and feeding on downward from the left. This will continue over the region where the pickets are exposed after which another layer of pickets will be inserted and winding of a reverse upward layer will begin.

Figure 14. Final view of the superconducting coil just before welding on outer stainless steel wall to seal the helium can. The coil leads form a tracklike pattern on the outer surface. A final test for grounds is being performed.

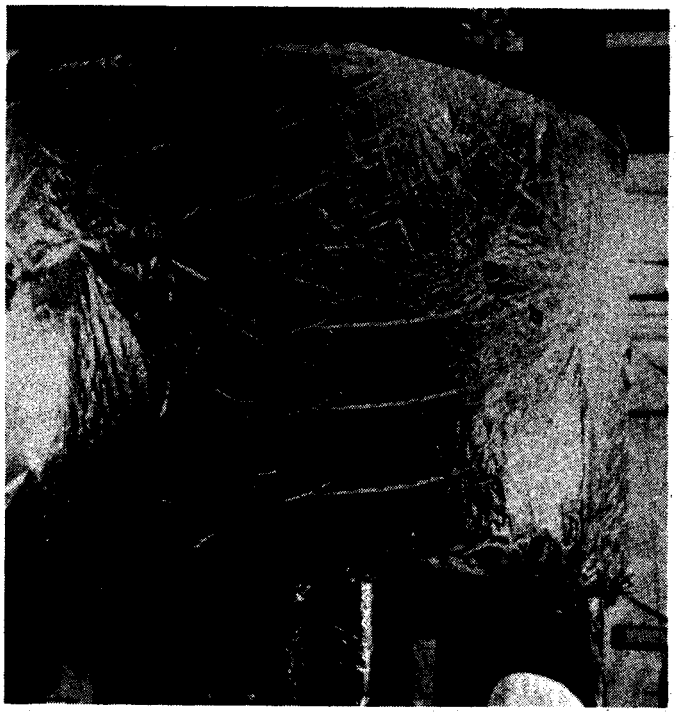

Figure 15. Photo of the coil after installation of aluminized mylar superinsulation.

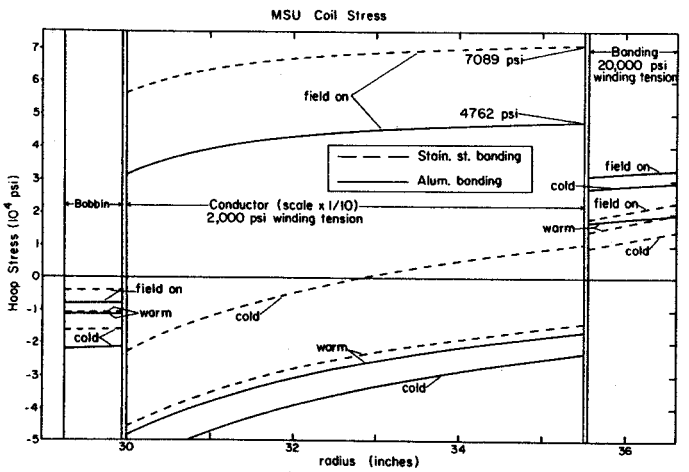

Figure 16. Calculation of internal stress in the coil assuming outer banding of stainless steel (dashed curves) and of aluminum (solid curves). The curves labeled "warm" give the stress distribution at the time winding is completed i.e., with the coil under compression due to the high winding tension in the outer banding and the bobbin under compression due to the winding tension of both coil and banding.(Note that stress curves for the coil are expanded ten fold relative to bobbin and banding.) Cooling the coil causes a redistribution of tensions due to differing thermal contractions of the several materials. Turning on the field gives a second redistribution of stresses as a result of the magnetic force on the conductor. Based on these calculations, aluminum banding was selected because it leads to a lower final stress in the conductor as a result of the greater contraction of the banding in the cooling process. Note that even though the"field on"condition leads to a positive stress in the conductor, the bobbin remains under compression indicating that the coil is still pressing in on the bobbin. No position shift of the coil relative to the bobbin should then occur.

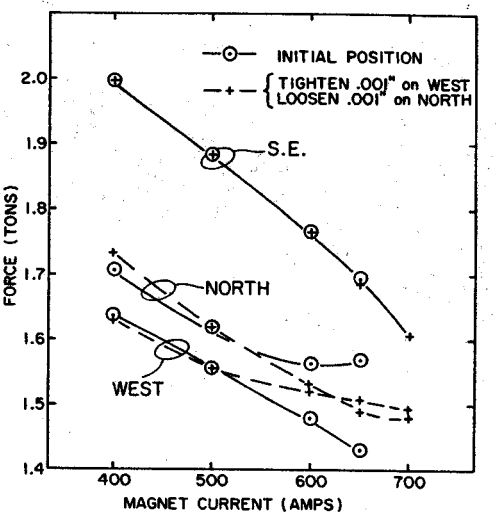

Figure 17. Experimental data from strain bolts in the three radial support links vs. magnet current. The run labeled "Initial Position" was terminated at 650 amps because the tension in the north link had ceased to decrease. The extreme sensitivity of the system is indicated by the second run in which a one mil change in the relative West/North position gives a large shift in the relative behavior of the two forces.

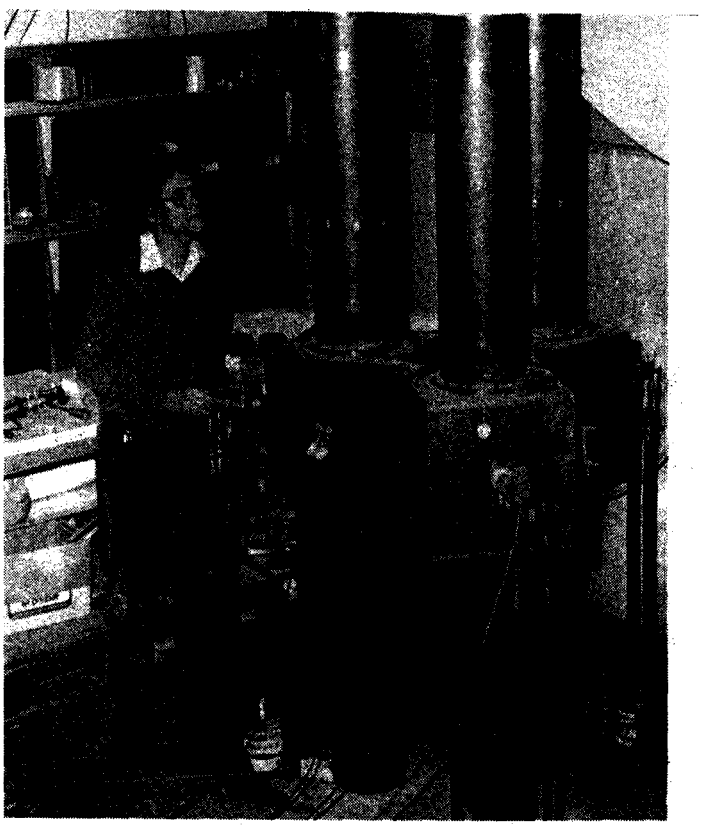

Figure 18. Photograph of high "Q" tuning model. Dees and dee-to-dee coupling are included as lumped elements. Dee stems, tuning servoes, and drive circuits correspond to actual structures which would be used in the completed cyclotron. Servo circuits were developed which accurately regulate the phase difference between dees to any desired multiple of 120°. Measured "Q" of the model is 6000.

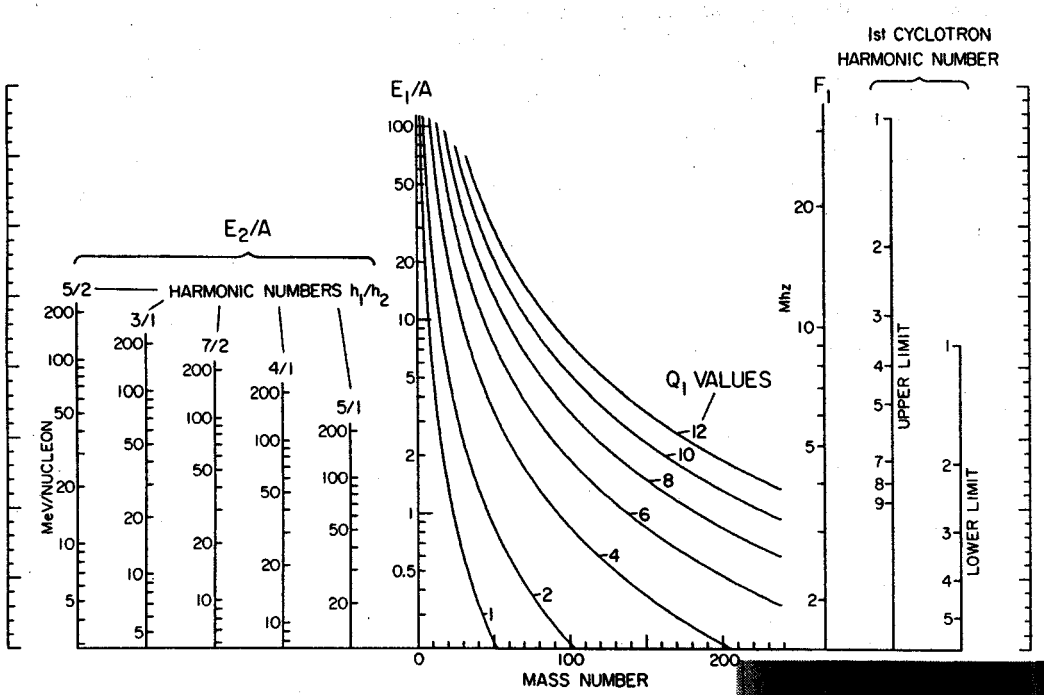

Figure 19. Energy multiplication and frequency plot when the first cyclotron is operating at peak field. A horizontal line reads out the orbital frequency in the first cyclotron, limiting energy for various values of the charge in the first cyclotron, and the energy from the second cyclotron for various values of the harmonic ratio. The two right hand columns give upper and lower frequency limits for various harmonics assuming the RF operates in the range 9 to 32 Mhz.

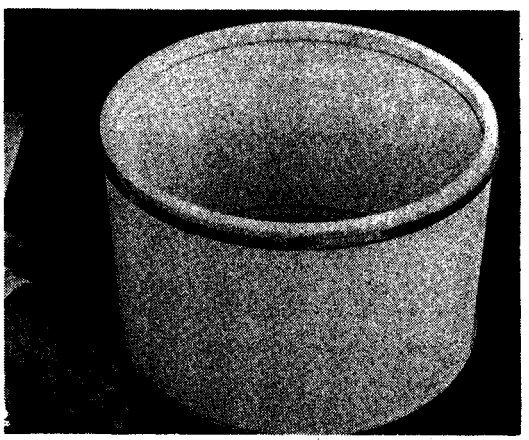

Figure 20. Photo of dee stem insulator fabricated from 99.5% alumina 10" high x 16" in diameter with 0.375" thick walls and with vacuum tight copper rings brazed at top and bottom for attachment to main vacuum wall.

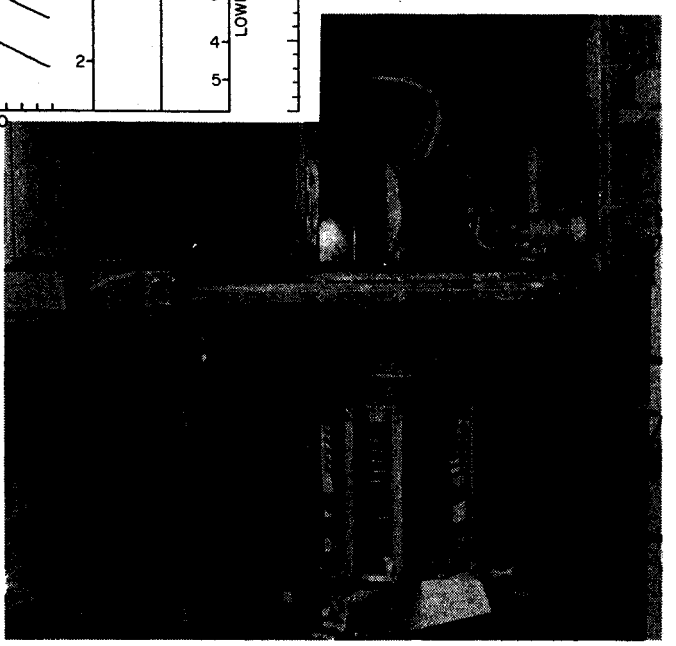

Figure 22. View of prototype RF amplifier. The grid box is at the top, the plate box at the bottom. The plate structure of the 4CW100,000 is visable just below the separating partition.

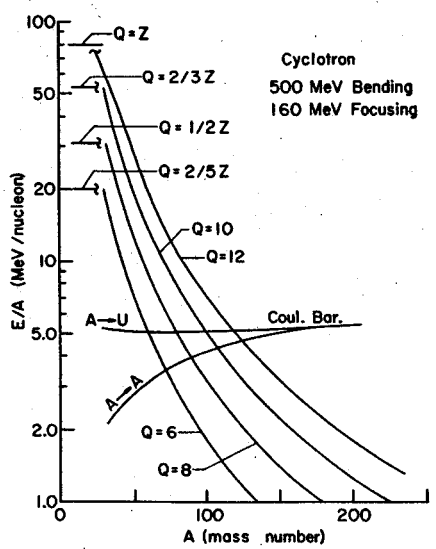

Figure 21. Energy per nucleon vs mass number for ions of various charge assuming the K500 is operating as a stand alone cyclotron.

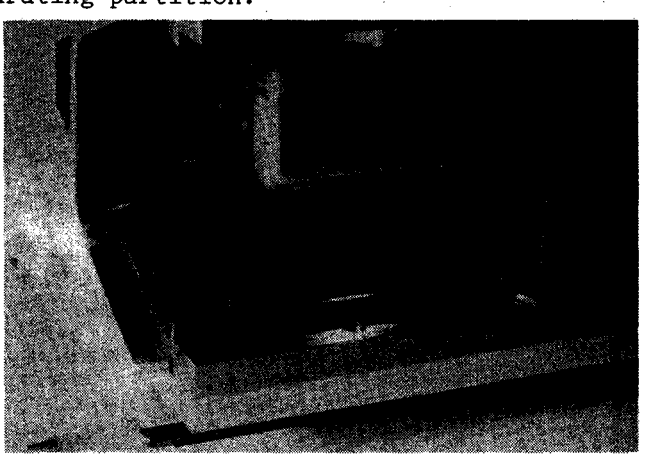

Figure 23. Photograph of deflector test assembly. Electrode cross section, clearances and insulators have the same dimensions as planned K500 deflectors. Tests in the 1.8 tesla magnetic field of the K50 cyclotron baked in easily to the power supply limit (electric field of 140 kV/cm).

Design of the Central Regions for the 500 MeV Cyclotron

E. Liukkonen, J. Bishop, S. Motzny, and T. Antaya

In the course of development, the frequency range of the 500 MeV cyclotron has changed considerably from the originally proposed range of 27-84 MHz, in which it was intended to operate in the third and nineth harmonic modes of acceleration. Detailed studies of this frequency range revealed two relatively serious sources of difficulties, 1) the large physical size of the dees causes a severe voltage gradient to occur along the dees when operated at high frequencies, and 2) a serious transit time effect between the ion source and puller was shown to exist on the higher harmonics. This second difficulty would force the use of a DC bias on the ion source, which is not desirable due to the expected maintenance problems. To overcome these problems a much lower frequency range was introduced, namely 9-32 MHz. This frequency range is excellent in the coupled operation of the 500 and 800 MeV cyclotrons, but it will require the 1st harmonic acceleration in the stand-alone use of the 500 MeV cyclotron for the most interesting high-energy light heavy-ions. This can be seen in Fig. 1a, which shows the required rf frequencies for maximum energies in h=1, 2, and 3 operations as a function of the charge to mass ratio, q/m.

Fig. 1b represents the energy gain which particles achieved between the ion source and puller electrode, when particles are extracted with 100 kV rf voltage in h=1, 2, and 3 harmonic modes using the maximum magnetic field. These curves are calculated with the source to puller part of the CYCLONE program (see a separate article in this Annual Report by M. Gordon et al.) using an electric field measured for the 50 MeV cyclotron (scaled here so that the minimum surface-to-surface distance is 10 mm to hold 100 kV). As can be seen in Fig. 1b the energy gain is nearly constant in h=1 mode, but decreases rapidly in h=2 and 3 modes with increasing q/m.

Fig. 1c displays the transit time (in rf degrees) between the source and puller. A feature worth noting is that in the h=1 mode the transit times are nearly constant for $q/m \geq 0.3$. This is due to the fact that the focusing limit of the 500 MeV magnet forces the use of lower magnetic fields for these particles at highest energies. Therefore the orbits of these particles are nearly identical, which allows the design of a central region with a fixed source-puller geometry in the h=1 operation.

The first central region studies for the 500 MeV cyclotron were made by J. Bishop in 1977 for the 3rd harmonic operation, when the 27-84 MHz frequency range was still under consideration. An electrolytic tank was built and a complete set of electric field maps was measured. This set of electric fields is used in many orbit calculations with a new CYCLONE program which is capable of handling the three phase operation. Although this first central region might only have academic interest in real applications, it has served well as a first approximation on which all later revisions are based.

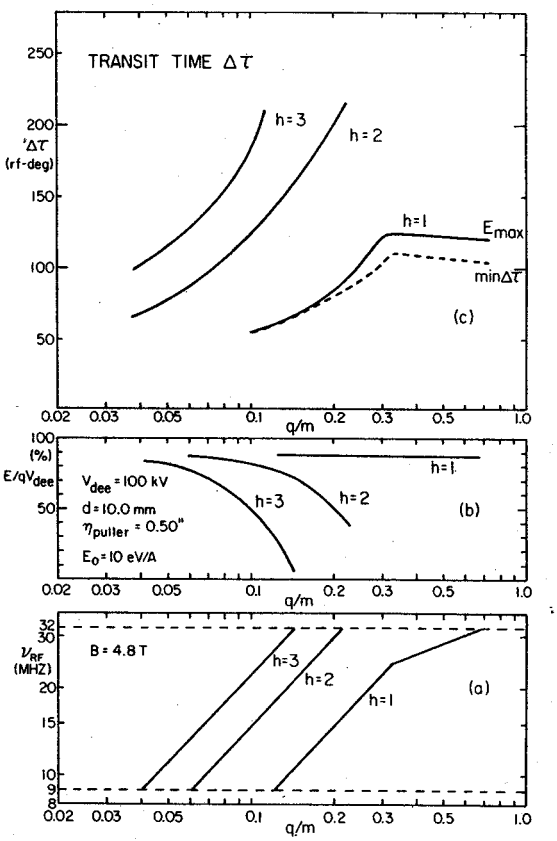

Fig. 1. (a) The required rf frequencies, (b) the energy gain, and (c) the transit times in the gap between the ion source and puller are plotted as a function of charge to mass ratio, q/m for the first, second, and third harmonic acceleration of particles in the 500 MeV cyclotron operating with the maximum magnetic field. For details, see text.

The introduction of the lower rf frequency range naturally shifted the design efforts to a central geometry suitable for the 1st harmonic acceleration. The orbit calculations showed, however, that the basic central geometry was not well matched for the 1st harmonic beams. Only a marginal clearance was left between the source and dee for holding the required dee voltage of 100 kV. (Building of two separate rf systems was already considered as a solution to this problem. Besides the "long" rf system, a "short" system was planned to cover rf frequencies from 32 to 60 MHz. Thus the 1st harmonic operation would

not be needed in the stand-alone use of the 500 MeV cyclotron.)

An effort was made to design a new central region to overcome the clearance problems. The dummy dee between dees #1 and #2 was cut shorter to allow locally higher energy gain and then also higher radial gain near the calculated position of the ion source. A new electrolytic tank was built, and electric fields mapped. Orbit calculations were repeated and adequate overall clearances and other desirable beam qualities were obtained. As an example, the calculated orbits of $^{28}Si^{9+}$ ions are drawn in Fig. 2, together with the superimposed equipotential contour lines. The position of the ion source was adjusted so that particles will have a positive phase of about 10^{o} when they arrive at the 1st acceleration gap at 90^{o}. The starting conditions indicated in the figure produce well-centered orbits. Also, the centering error due to the different starting times was found to be reasonably small. The orbits of particles having lower change states were also checked and the electrodes designed so that these undesirable beams can be stopped as early as possible, normally during the first turn. The h=1 geometry was also studied using our other "standard" beams: $^{14}N^{4+}$ (q/m=0.286, E=41 MeV/A), $^{2}H^{1+}$ (q/m=0.498, E=81 MeV/A), and $^{3}He^{2+}$ (q/m=0.666, E=107 MeV/A). All of these particles produced well-centered beams using the same source-puller geometry as in Fig. 2.

The success with the h=1 geometry has now removed the need to build the second "short" rf system.

The coupled operation of the 500 and 800 MeV cyclotrons required that the 500 MeV cyclotron should mainly operate in h=3 and 4 modes. As can be seen in Fig. 1c the use of an rf extracted ion source will be restricted only for beams with low q/m-values (if max. B-field is used) due to the transit time effect. On the other hand, the beams with the low q/m-value will have only a very small number of turns in the 500 MeV machine, e.g. 44 turns for $^{238}U^{10+}$ and 110 turns for $^{75}As^{8+}$ (with V_{dee}=80 kV). These low turn number beams will require that the ion source be placed at a relatively large radius (r=1.0"-1.8"), causing an

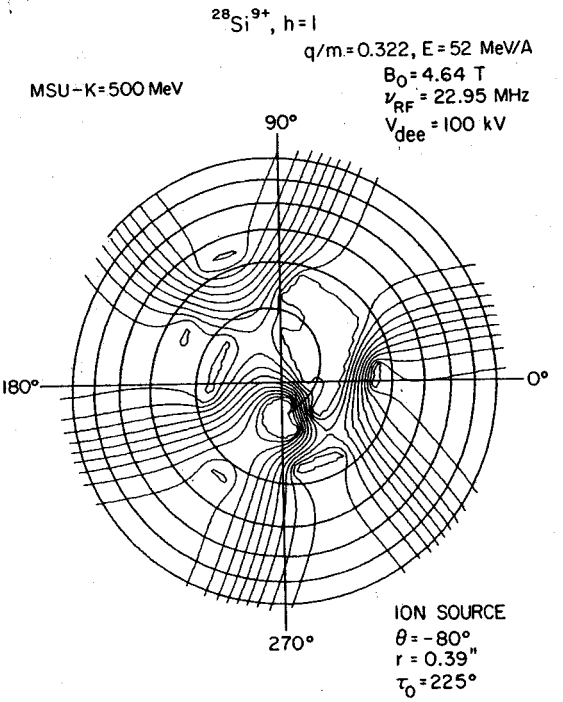

Fig. 2. Equipotential contours of the central region designed for the first harmonic operation of the 500 MeV cyclotron, together with calculated central-ray orbits of the $^{28}Si^{9+}$ ions.

undesirably large dip in the magnetic field. To overcome these problems different solutions are being considered. One can use a grid on the ion source in order to solve the transit time problems but the grid will not help for the large starting radius. A DC-extracted ion source in the center of the magnet is one possibility. The expected intensity problems with this type of ion source can be serious, however. The axial injection is also an open possibility. Studies of these various options are continuing.

Beam Extraction Studies for the K = 500 Cyclotron

M. Gordon and E. Fabrici

In last year's annual report, a detailed account was presented of the problems and procedures associated with the design of the extraction system. Most of the changes in this design which have occurred during the past year were dictated by revisions in the rf system. The new frequency range, 9 MHz to 32 MHz, requires first harmonic acceleration for many important ions produced in the stand-alone operation of the K=500 MeV cyclotron. As pointed out in last year's report, first harmonic acceleration presented certain difficulties which required further study. These studies have now been carried out, and the resultant design changes appear to have overcome the difficulties.

Fig. 1 shows a schematic layout of the extraction hardware according to the current design. There are threeelectrostatic deflectors (E1, E2, and E3) and two sets of focusing bars (F1, F2) with the second set divided into five subsets (F2,1-F2,5). A detailed description of these focusing bars and their properties was presented last year. An important design change here has been a reduction of the aperture from a=0.64 to a=0.50 inch, which raises the focusing gradient to 9.6 kG/inch and the central field decrement to 0.89 kG. The feasibility of this aperture decrease was confirmed during a detailed study of the beam optics in the extraction system (see below). This study also produced the final design for the number and distribution of the focusing bars F2.1 to F2.5 shown in Fig. 1.

The fringing field of the focusing bars is sufficiently strong in the region occupied by the beam prior to extraction that it may produce an undesirable disturbance of these orbits. This disturbance arises from the first harmonic component of the fringing field which may produce a large and difficult to control orbit displacement as the beam accelerates through the $\nu_r=1$ resonance prior to extraction. In order to minimize this effect, two sets of compensating bars (C1, C2) are introduced as shown in Fig. 1. The sets C1 and C2 are designed to cancel as effectively as possible the first harmonic produced by F1 and F2, respectively. As noted in last year's report, we had thought it sufficient simply to produce a perfect cancellation at the position of the $\nu_r=1$ resonance (r=25.7 inch). Although the resultant perturbation was sufficiently controlled to permit good beam extraction with third harmonic acceleration, it proved much too strong for first harmonic acceleration (which requires twice as many turns) and led to a premature entrance of the beam into the extraction channel.

This problem has been solved by the new F1 design which merges the two sets of focusing bars

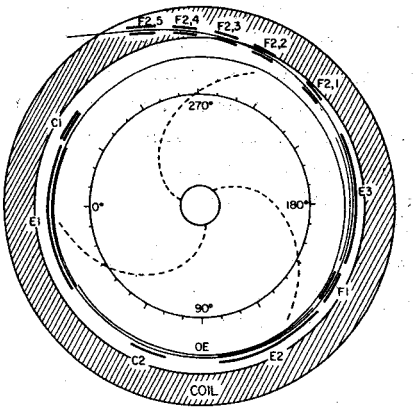

Fig. 1. Schematic layout of the extraction system. The elements shown are three electrostatic deflectors (E1, E2, E3), two sets of focusing bars (F1, F2) with the second set divided into five subsets (F2.1-F2.5), and two sets of compensating bars (C1, C2). E1, E2, and E3 occupy the theta intervals: -24° to $+32^\circ$, 96° to 138°, 158° to 206°, respectively, and all three required only 92 kV/cm to successfully deflect the central ray orbit shown. All of the focusing bars have the same aperture a=0.50 inch, corresponding to a focusing gradient of 9.6 kG/in., and a field decrement of 0.89 kG along the beam axis. F1 occupies the interval $\theta=142^\circ$-154°, while the sets F2.1-F2.5, each of which has $\delta\theta=8^\circ$, occupy the region beyond $\theta=220^\circ$. C1 is identical to F1 and located 180° away, so that these two produce no first harmonic field at all; C2 is positioned at $\theta=62^\circ$-76° and is designed to compensate for the first harmonic produced by F2.

The curve labeled OE represents the envelope of all the internal orbits prior to extraction. The two large circles (r=30" and 36") indicate the boundaries of the superconducting coil. The three broken spiral curves show the centers of the three magnet hills. Scale markings for the azimuthal angle θ are shown on a reference circle at r=20". The central ray extraction orbit shown here was calculated for an ion with q/A=0.31 having a final energy of 49.4 MeV/A in the magnetic field with B_o=47.4 kG.

previously occurring before and after E2, and which situates the resultant F2 more advantageously. This new position allows C1 to be located exactly 180° away, as shown in Fig. 1. The new C1 is identical to F1, and by symmetry, these two elements produce no first harmonic at all. The entire perturbation is therefore produced by F2 and C2 which are at larger radii and hence weaker in effect. The resultant first harmonic is less than 1.0 gauss over the region occupied by the accelerating beam, whereas the corresponding value for the old design was 23.4 gauss. As noted last year, the second harmonic gradient perturbation can also produce troublesome effects, and we should note here that the

value of this gradient in the new design is less than half that obtained from the old one.

The orbit calculations required to establish a central ray and associated paraxial rays for the extraction system were described last year. These procedures have been followed again using the main field with B_o=47.4 kG, together with the field perturbations produced by the focusing and compensating bars. Starting at E/A=40 MeV with an ion having q/A=0.31 and using first harmonic acceleration to determine the central ray orbit, we obtained E/A=49.4 MeV for the extraction energy, which matches the design goal very well. The resultant central ray orbit was then successfully tracked through the extraction system using only 92 kV/cm on all three electrostatic deflectors, which is significantly lower than the 100-120 kV/cm required previously. The new central ray orbit is the one shown in Fig. 1.

In addition to the central ray, two sets of accelerated orbits were calculated starting with initial displacements on an (r,p_r) and an (z,p_z) eigen-ellipse, respectively. The radial eigen-ellipse was chosen to have a width δ_r=0.1 inch at 40 MeV, which corresponds to a final emittance of 6.9 mm-mrad (about three times the emittance from our present cyclotron). The axial eigenellipse was determined by choosing δ_z=0.4 inch for the maximum beam height at 40 MeV, which corresponds to a final emittance of 7. mm-mrad. The resultant phase space areas at 49.4 MeV were then tracked through the extraction system. Fig. 2 shows the final results obtained after making a series of adjustments on the subdivisions of F2 in order to optimize the resultant beam optics. As can be seen, the radial and axial beam widths are extremely well behaved throughout the extraction system. The radial beam width never exceeds 0.24 inch while the vertical width remains less than 0.4 inch.

Fig. 2 also shows the results of a dispersion calculation obtained by tracking two orbits through the extraction system whose initial conditions match the central ray in all respects except that they have δE/A=±50 keV, which corresponds to an energy spread $(\Delta E)/E=1/500$. As can be seen, these two rays move steadily apart and reach a final separation of 0.39 inch at $\theta=308^o$ where r=38 inch. Although the gradients of the focusing bars help to counteract this dispersion, their effectiveness here is rather limited.

We should also point out that the final configuration of focusing and compensating bars is not the same as the one used to calculate the field perturbations on the accelerated orbits in the pre-extraction region. The entire design procedure should therefore be iterated until complete self-consistency is achieved, which could be quite tedious. Fortunately, reasonably accurate analytical estimates indicate that the changes in the field perturbations should have a negligible effect.

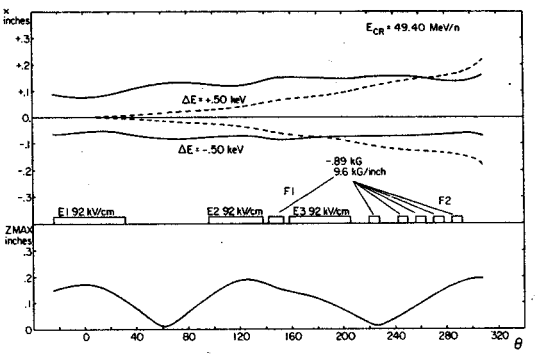

Fig. 2. Focusing and dispersion properties of the extraction system. The two solid curves at the top show the envelope of the radial displacements for a set of orbits tracked through the extraction system. These orbits originate on an eigen-ellipse centered on the central ray (shown in Fig. 1) with a total radial emittance of 6.9 mm-mrad. The two broken curves at the top illustrate the dispersion arising from two orbits which differ in energy by ±50 keV out of 49.4 MeV/A, but which otherwise match the central ray. At the bottom is a plot of the maximum z values for the linear vertical oscillations of a set of orbits which originate on a (z,p_z) eigen-ellipse corresponding to an emittance of 7. mm-mrad. Between these plots are symbols marking the locations of the three electrostatic deflectors and the various sets of focusing bars described in Fig. 1.

Operating Experience of the Superconducting Magnet Cryogenic System

Merrit Mallory

The past year of operating experience with cryogenic system of the superconducting magnet has resulted in increased understanding of the magnet cooling requirements and its operation with liquid helium. In particular a method was developed for finding small helium leaks between the cryogenic vessel of the magnet and its vacuum jacket while it contained liquid helium. The method utilizes the temperature variation of the viscosity and density of cold helium gas as shown in Fig. 1. Changes in the temperature of the

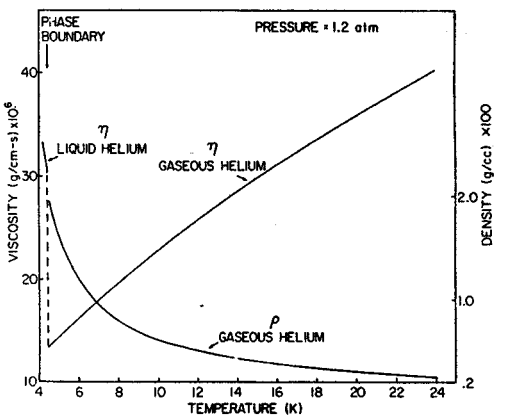

Fig. 1. The viscosity and density of helium from 24 K to 4 K at a pressure of 1.2 atm, the operating pressure of the superconducting cyclotron cryostat, are shown. A temperature change from 24 K to 4 K causes a change in the helium viscosity of ≈3 and hence a corresponding change in the leak rate through a crack.

helium gas at the leak location cause changes of the leak rate into the vacuum jacket. Several ways of temperature variation of the cryostat are possible, but the method used here has utilized the fact that ten different connections to the helium refrigerator exist and the boil-off gas from the liquid helium (≈5°K) can be returned from any one of these ten connections for short periods. The change of the boil-off return gas causes a temperature shift in the cryostat and corresponding variation in the vacuum jacket pressure, which then can be used as indications of leak locations. Fig. 2 is an example of the effect when cold helium gas was allowed to flow through current lead number one and clearly shows a helium leak. Three additional helium leaks have now been found by this technique. As the helium leaks of the cryostat have been fixed, the helium consumption of the magnet has decreased to ≈9ℓ/hr. (≈within a factor two of the theoretical value). This leak detection technique offers the potential of finding leaks at liquid helium

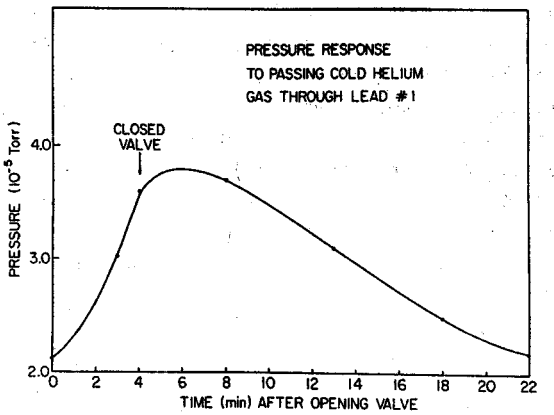

Fig. 2. Measurement of the pressure in the cryostat vacuum jacket when cold helium gas is passed through the cryostat area containing the crack. Additional leaks have now been found with leak rate five times smaller than the one shown above.

temperatures that have leak rates three magnitudes smaller than presently achieved at room temperature.

The helium leak in the cryostat has also allowed measurements of the "hold-up" time at room temperature of helium atoms in the super insulation layers surrounding the liquid helium can. The helium leak detector is used to monitor the cryostat vacuum jacket (containing 27 layers of super insulation, 27 layers of paper, and the liquid nitrogen shield) and it detects a helium leak rate of $\approx 1 \times 10^{-9}$ torr ℓ/sec., while the pressure in the vacuum jacket is held at $\approx 1 \times 10^{-3}$ torr by a 6" diffusion pump. The warm helium gas is then evacuated from the liquid helium can, thereby removing the helium leak source. After approximately 60 minutes, the leak detector does not see any helium atoms (sensitivity of $\approx .5 \times 10^{-10}$ torr ℓ/sec.) indicating that they have been completely pumped from the super insulation layers.

In filling the cryostat with liquid helium, a chocking mode on the transfer rate has been detected. Normally, liquid helium is introduced at the bottom of the cryostat and it easily fills up to the top of the coil windings. At this point the helium fills a reservoir above the coil. Difficulties in filling this reservoir had been encountered originally and we would finally succeed after several days and trying many things. In one of the attempts at filling this reservoir, it was recognized that the liquid helium refrigerator was making large quantities of liquid helium and a factor of two change in pressure

on the liquid helium feed dewar made no change in helium height in the cryostat reservoir. Changing the liquid transfer line to the top fill port of the cryostat then resulted in immediate filling, after passage of the heat pulse, and this procedure has now been adopted.

The helium level sensor in the refrigerator port of the cryostat has responded differently than the other level sensors when liquid helium was introduced into the cryostat through the top liquid helium fill port. Namely, the level sensor has given indication that liquid helium was filling that port up to the 80% level, when all other information indicated no liquid helium in the top of the cryostat. In examination of the drawings, it was found that the helium splash baffle, located directly under the liquid helium top fill entrance, appears to be in close contact with the level sensor at the 80% mark. It is postulated that the liquid helium forms a pool on top of the splash baffle and then flows from the pool down the level sensor and into the cryostat, thereby making it appear to the level sensor that it is under liquid helium. We conclude from this data the path that the liquid helium is following in the cryostat from the top fill port. Secondly, that the refrigerator level sensor is really measuring the fact that liquid helium is flowing into the cryostat, and finally, that with an appropriate design these level sensors could be used to monitor liquid helium flow.

In summary, the past year we have gained a better understanding of our cryogenic system and expect to continue learning more about details in the coming year.

Ion Source Operation in the Superconducting Magnet

Merrit Mallory

A cold cathode heavy ion source was operated in the superconducting magnet on June 22. The source, also used in the K=50 cyclotron, was initially struck at a magnetic field of ≈20 kG, with nitrogen as the source gas. The magnetic field was then increased to its maximum value (≈50 kG). No changes in the arc parameters or the glow discharge, as observed through a window in the vacuum chamber, were noticed. The arc gas supply was decreased until the arc unstruck. The arc was then easily restruck at the 50 kG level.

Subsequent operaion of the ion source has revealed one interesting result. In normal arc operation, the ion source voltage first increases to ≈4.5 kV and <.5 A arc current (mode 1) and then the arc is said to strike. Namely, the arc voltage drops to ≈500 volts and the arc current increases to 2-5 Amps. (mode 2).

In mode 2, the high charge state heavy ions are observed and a glow discharge is seen in observation of the ion source slit. Normally, a glow discharge is not observed in mode 1. At high magnetic field levels, a glow discharge is now observed at the ion source slit in mode 1 and it appears to be as intense as in mode 2.

Fig. 1 is a picture of the dc electrode that is being installed in the 50 kG magnet and it will perform charge state analyses of the ion source plasma. The electrode is designed to operate at 30 kV and analyze m/q ratios greater than 5. In summary, the heavy ion source operates very well in the 50 Kg magnetic field.

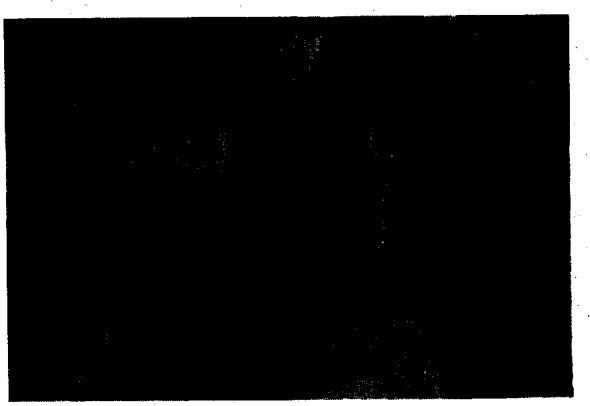

Fig. 1. A picture of the dc electrode used to extract the beam in the K=500 cyclotron. Only m/q ratios greater than 5 can be analyzed at 30 kV.

Magnetic Field Measurements in the 500 MeV Magnet

P. Miller, H. Blosser, D. Johnson, D. Gossman, P. Marchand, B. Jeltema, and M. Mallory

The apparatus described in the 1976-77 Annual Report was employed to map the field of the 500 MeV magnet. The azimuthal scanning was done with a stepping motor coupled to a worm drive. The stepping motor required a 3 layer cylindrical magnetic shield to keep it from stalling in the fringe field near the yoke at full magnet excitation.

The magnetic field $B=k\Delta W$ is inferred as the product of the coil-integrator calibration constant k and the average integrator voltage change for two flips (one up and one down). Thus, a linear integrator drift is cancelled. (Typical integrator drift rate is 0.1 mV/sec.; the time between measurements before and after a flip is about 20 sec.). To correct for temperature changes one would multiply k by the factor

$$(1 + C_E \Delta T_E - C_C \Delta T_C),$$

where the last two terms refer to the coils and the electronics, and the ΔT's represent temperature changes relative to the temperature at the time the calibration constant k was determined. Average values of the experimentally measured coefficients are given in Table I. All units have similar coils, with 16 Ω resistance.

The table shows that two different size feedback capacitors were used in the integrators. The average noise, as measured by the rms fluctuation in the values obtained from repeated field measurements, is slightly lower in the type 2 integrators. Because the temperature fluctuations during mapping were small ($\simeq 1^{\circ}C$) the temperature corrections were not included in the computer program, although temperature data were recorded with the feild maps automatically. Also, the integrators appeared to be linear to within 0.03% in their response to magnetic field in the calibration magnet over the range 1.5 to 3.8 kgauss where absolute NMR measurements were available. A computer program to make repeated measurements with the arm azimuth fixed showed that the magnetic field drifted downward in all measuring coils by 6 gauss in one hour. This effect as well as any uniform temperature drift was corrected in the analysis of each map by normalizing the measured points to make the central field constant.

Field maps were obtained with the two sections of the main coil excited to currents shown in Table II. The Fourier components for several maps were compared to those from a field distribution calculated by Blosser and Johnson.[1] Some small discrepancies ($\simeq 1\%$) in the average field profiles were traced to details of the iron distribution which were not included accurately in the original calculation. The calculation itself was refined, as described below, to make the geometrical representation of the steel in the calculation more realistic. When these corrections were made, the agreement was within 0.3% in the 700 A average field. The measured average field vs. radius is plotted in Fig. 1, and the deviation of the calculated field from the measurements is plotted in Fig. 2. Note that each radial position corresponds to one flip coil location. The peak structure that appears in all three sets of data is probably a measure of the relative calibration errors among individual flip coils ($\pm 3 \times 10^{-4}$). The vertical translation of the curves can be caused either by inaccuracy of the calculation or by a calibration error (e.g. gaussmeter temperature effect or power supply current).

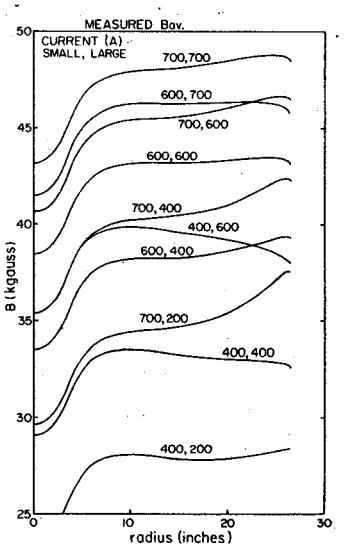

Fig. 1. Radial profile of the average magnetic field measured in the 500 MeV magnet for various combinations of currents in the two sections of the main coil.

Table I. Typical Fluxmeter Properties

Type	Integrator Components	Number of units	ΔC_C ($^{\circ}C^{-1}$)	ΔC_E ($^{\circ}C^{-1}$)	Average Noise (T)	Average k ± S.D. (T/V)
1	.022 μf 1M	41	9×10^{-5}	3×10^{-4}	$.9 \times 10^{-4}$	.675 ± .020
2	.1 μf 220K	14	5×10^{-5}	8×10^{-5}	$.6 \times 10^{-4}$	.672 ± .012

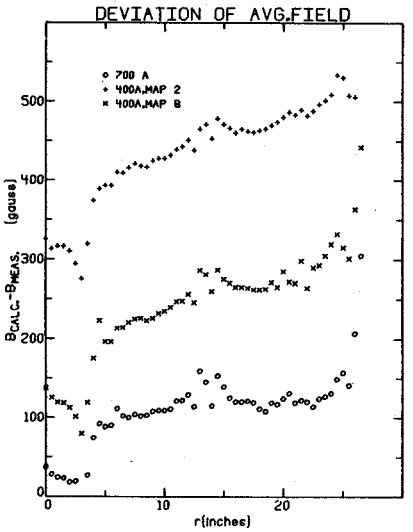

Fig. 2. Radial profile of the average magnetic field calculated by the procedure described in the text.

Table II. Main Coil Currents

Map. No.	Small Coil (A)	Large Coil (A)
1	498	498
2	400	400
3	600	600
4	700	700
5	200	200
8	400	400
10	600	700
11	700	[illegible]
12	700	400
13	700	200
14	400	200
15	600	400
16	400	600

The refined magnetic field calculations make use of the ability of the relaxation code to calculate with different magnetic permeability in different places. This allows the radial and axial boundaries of the steel to be entered accurately. The azimuthal structure is treated by scaling the magnetization to the fraction of the volume occupied by steel. This is implemented approximately, due to numerical limitations of the code, by dividing the steel into a few regions, each with a constant scale factor, as shown in Fig. 3. Since the spaces in the iron do not have constant angular width, average scale width, average scale factors are used. This approximation is corrected, however, by superposing the saturated iron field from the small regions ignored by this simplification, as well as the nonsymmetric parts due to the actual holes and spaces in the steel, as described in Ref. 1.

The third harmonic amplitude B_3 in the 700 A measured field was within 5% of the calculation and the sixth harmonic differed by 7 to 15% from

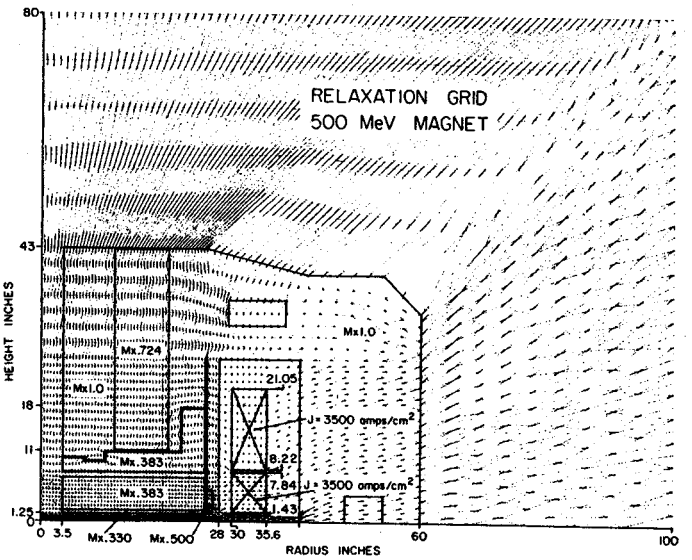

Fig. 3. Grid used in the relaxation calculation of the circularly symmetric portion of magnetic field. The magnetization M inferred from the B vs. H curve for 1020 steel is multiplied by different normalization factors in different areas to represent the fraction of the volume occupied by iron.

its corresponding value. The overall agreement between calculation and measurement implies that detailed orbit calculations can be carried out in fields generated from the calculation procedure. This avoids the common difficulties associated with smoothing and interpolating in measured field maps.

The first harmonic amplitude obtained from the analysis of two maps is plotted in Fig. 4. This harmonic is the most important imperfection because the orbit center is sensitive to this component at the crossing of the $\nu_r=1$ resonance. The amplitude B_1 is presented in the figure as a fraction of the average field because this parameter relates to the effect on the beam.

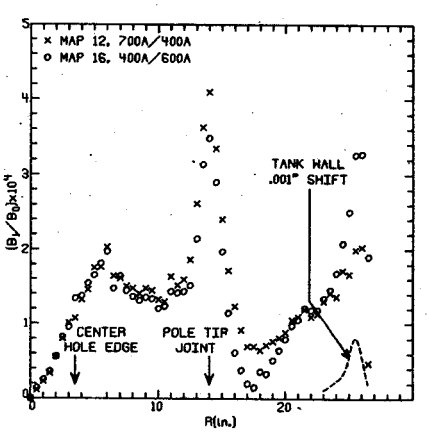

Fig. 4. Radial profile of the first harmonic amplitude B, expressed as a fraction of the average field B_0 for two typical maps. The calculated curve giving the effect of a .001 inch centering error of the coil was normalized for an average field of 40.8 kgauss. Comparison of this with the data implies that there is a centering error of about .003 inch.

A large peak near r=14 inches, where there is a joint in the pole pieces, indicates a misalignment of these parts. Some mechanical difficulties were noticed when the pole tips were installed, but rather than wait for construction of the redesigned spacers, the assembly was finished with the available parts. We expect that the problem can be corrected when the pole tips are removed to install the trim coils.

A smaller peak which has a shape and location resembling that inferred from the coil tank field gradient is presumably due to a centering error of that structure. The amplitude of the first harmonic is proportional to the centering error. There is some indication in these data of a shift in the coil tank position between the times the two maps shown were measured. It is even possible that the shift is induced by the change in current distribution in the two coil sections.

The consistency and smoothness of the phase angle is a good indicator of true field components. In Fig. 5 we show the amplitude and phase of both the first and second harmonics for the same two maps as in Fig. 4. The repeatability of these independent measurements implies that the harmonics are in the field and are measured accurately. The peak in B_2 near r=26 inches is expected, since the coil tank has a machining error which makes it out-of-round by 0.030 inch.

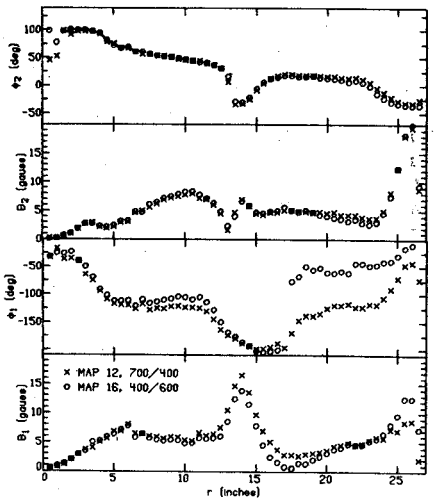

Fig. 5. Amplitude (B) and phase (ϕ) of first and second harmonics.

Following completion of the ion source and rf tests which use it, the magnet will be disassembled to install trim coils, extraction elements, and a central steel plug. Further mapping will be done to determine the effects of these modifications.

---

1. H.G. Blosser and D.A. Johnson, Field Calculations for the MSU 500 MeV Superconducting Magnet, MSUCP-28 (1977).

R.F. System

J. Riedel, R. Burleigh, W. Gress, D. Lawton, and S. Francis

Considerable evolution in the design of the r.f. system has occurred since the previous annual report was written. The most important changes in the r.f. structures result from a decision to first build an r.f. system to cover the frequency range 9 to 32 MHz, a proper range for the 500 MeV machine when it is to be used as an injector into the 800 MeV cyclotron. To tune the dees to 9 MHz requires stems 17 ft. long. The mechanical problem of supporting the dees on 17 ft. long 4 inch diameter pipes was solved by deciding to support the dees on 5 ft. long 4 inch diameter stems by using a 99.5% pure alumina insulator. This insulator is an exact copy of the insulator in use on the FNAL cavities and performance figures from FNAL indicate that it should be able to perform satisfactorily for us. Below the insulator the moving short is in air and can be moved with push rods. In addition to providing water cooling we will blow air by the fingers, thus increasing the likelihood that they will perform satisfactorily. Fig. 1 shows, in cross section, the upper half of one dee-stem structure.

After it has been demonstrated that the 500 MeV cyclotron, equipped with the above r.f. structure will perform satisfactorily as an injector into the 800 MeV machine, it may be desirable to modify it so that it can more effectively be used as a stand-alone cyclotron for nuclear physics experiments during the time the 800 MeV machine will be under construction. The appropriate frequency range for this use would be from 30 to 60 MHz. This can be accomplished by going back to the previous design: sliding short in vacuum

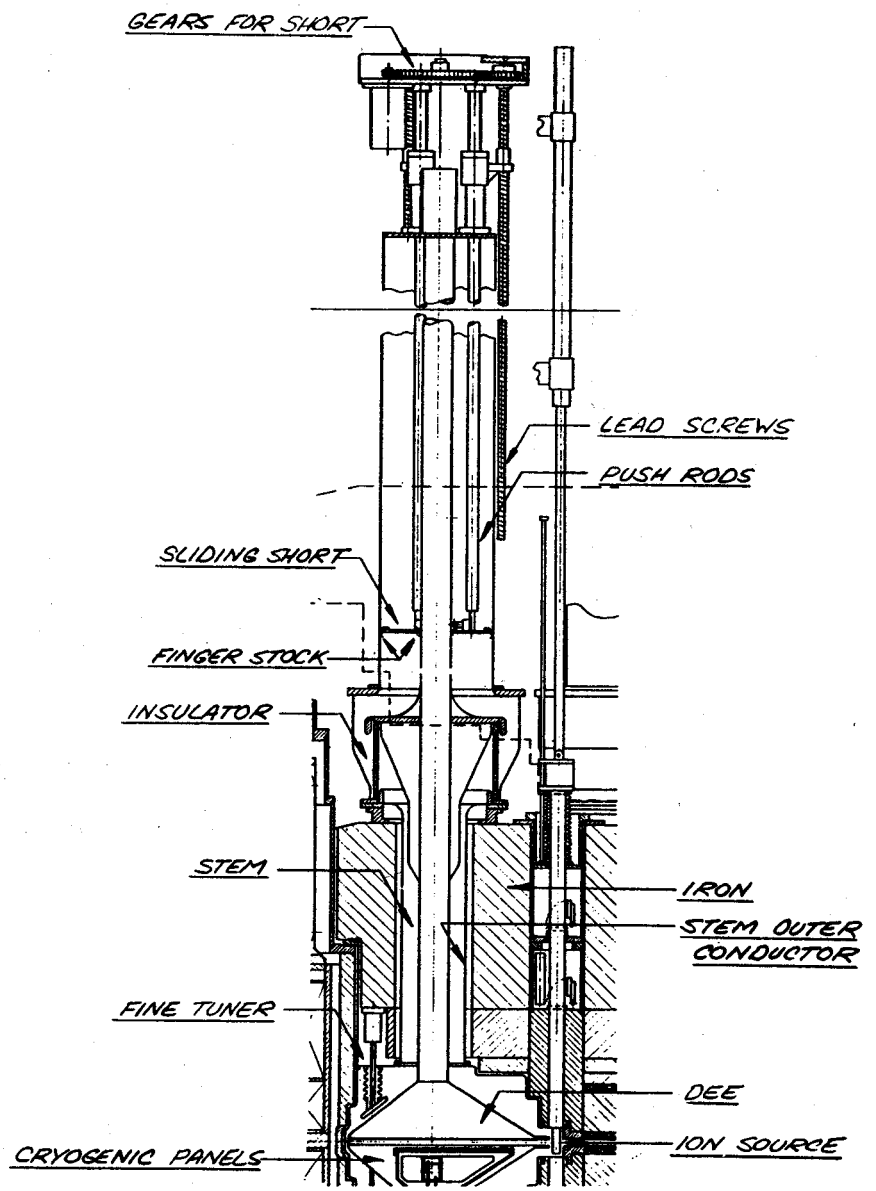

Fig. 1. Cross section of upper half of r.f. structure.

moving along five foot stems. It would thus be very similar to the Chalk River design.

Transmitter

The transmitter is being constructed and first tests are scheduled for October 1978. The 1kW driver has already been tested and performs well.

Overall Scheme

Fig. 2 is a block diagram to illustrate the overall scheme for the r.f. system. Although SE6A, B and C, which control the fast dee tuners, will be sufficiently fast and sensitive to provide for good efficiency in driving the dees, the requirement of 0.2 degrees phase stability will be met by SE1A, B and C which control the fast phase shifters.

Test Stand

To test the low level system, the transmitter, the insulator and the moving short, a test stand will be constructed. In this stand a vacuum box will house a structure to simulate a dee and it will be supported top and bottom by the final stems and insulators. Beyond the insulators, the final stems and moving short structures will be installed and the prototype transmitter will drive this structure. Thus, practically everything will be tested. It is hoped that these tests can be completed before January 1, 1979. If all goes well, it may be possible to have the complete r.f. system constructed and ready for tests by August 1979.

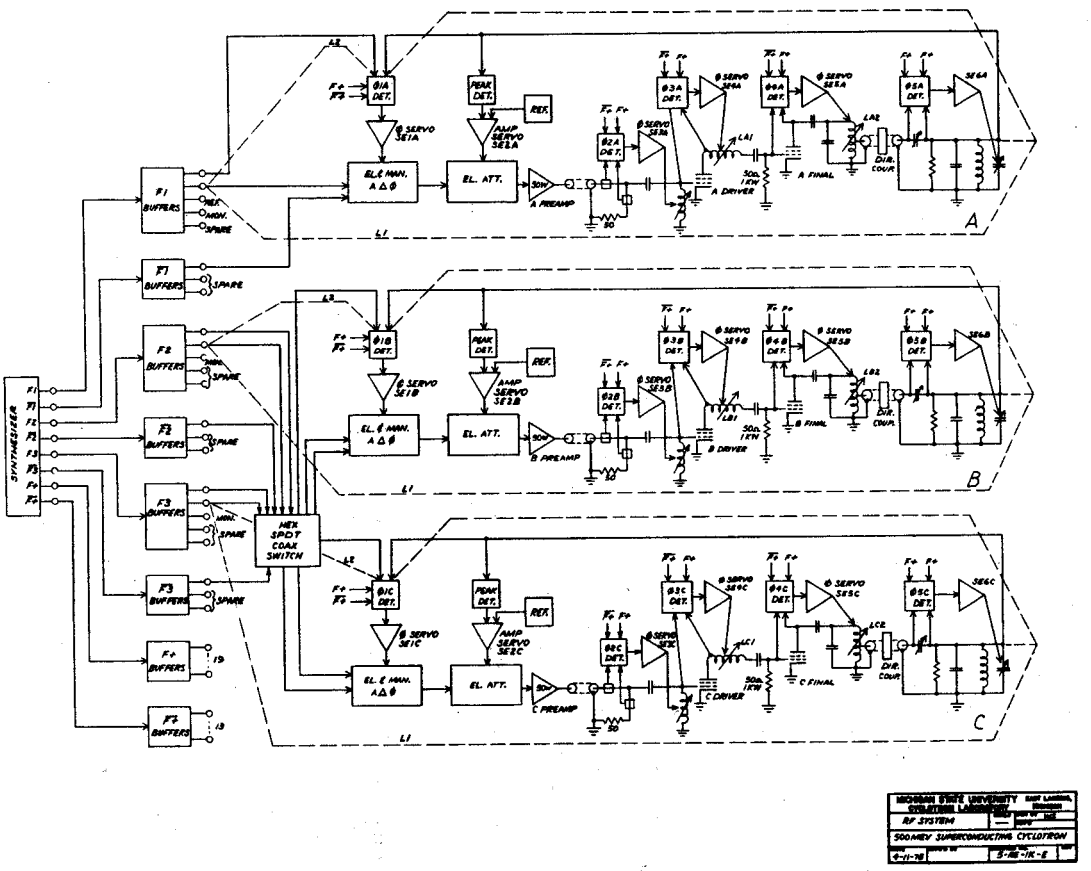

Fig. 2. Block diagram of r.f. system

Power Supplies for the 500 MeV Cyclotron

J.F.P. Marchand and W. Dumond

The D.C. power supply for the superconducting magnet coil was constructed in house and is now operating. The D.C. power supplies for the trim-coils are in development.

Main Magnet Power Supply

This supply is a dual 770 A @ 10 V precision current source for the superconducting magnet coils (Fig. 1). The supply has two identical power sections of classical design. The raw D.C. power is derived from the 440 three-phase line with a variac, step down transformer and diode rectifier. A water cooled pass-transistor bank provides for regulation. The output current is determined with a water-cooled shunt. The feedback regulation of the output current uses a chopper stabilised amplifier (AD234L) and a 16 bit precision digital to analog converter (DAC16QM). An Imsai 8080 micro-computer is built into the supply cabinet and provides for the control of all internal functions. This computer uses an Intel 8080 micro-computer integrated circuit. The control program was written in machine language and resides in 4 k-bytes of programmable read-only memory. The operator controls the supply with a digital control panel (Fig. 2). This panel displays the current on two 5-digit numeric readouts. The desired currents can be set by two 5-digit thumb-wheel switches and a strobe button. The output currents will ramp to the desired currents so as to reach the desired currents in both coils at the same instant, regardless of the previous operating condition. The ramp speed of the fastest slewing output can also be set by the operator, within the constrains of a ± 20 volt compliance voltage.

In case of power supply failure or interlock, an output shorting contactor provides a path for the magnet current, causing the current to circulate rather than forcing an inadvertent current dump.

Some work on the regulation circuitry still needs to be done in order to improve stability of the output current (estimated at 1.3×10^{-4}/hr).

Trim coil power supplies

A prototype of a 600 A @ 10V D.C. current regulated power supply for the trim coils is now (Aug. 1978) being built (Fig. 3). It is a so called 20 kHz switching power supply. The 208 V, three phase line voltage is directly rectified into a D.C. voltage, without an isolation transformer. This voltage is then converted to a 20 kHz square wave with a transistor commutator. A ferrite core transformer and fast recovery diode rectifier is then used to convert to low voltage D.C. output. Regulation is achieved by controlling the conduction duty cycle of the commutator. The advantages of this scheme are found in a reduction of transformer size and increase in supply efficiency. An increase in complexity, and maybe reliability, is a disadvantage of this approach. The supply will have a regulation of better than 1×10^{-3}.

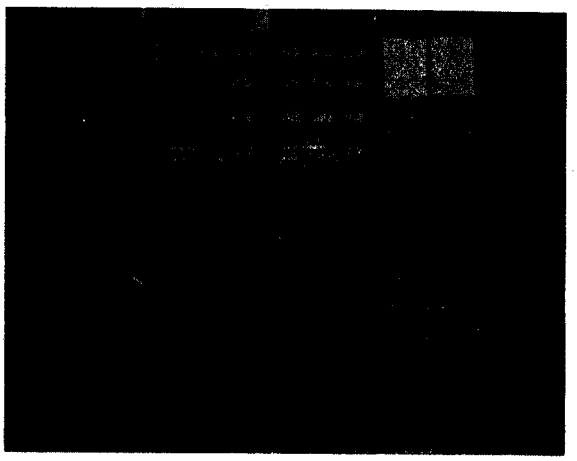

Fig. 1. The D.C. power supply for the superconducting magnet.

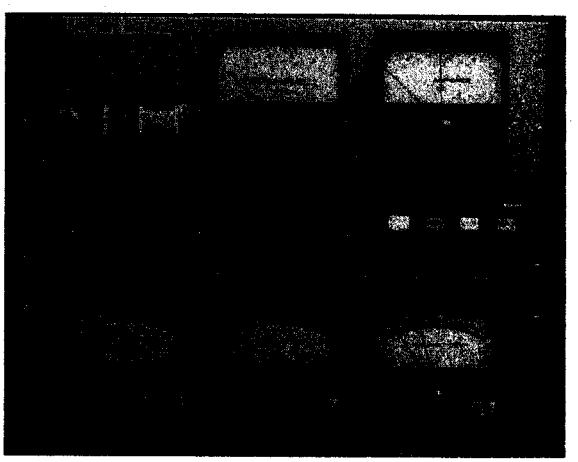

Fig. 2. Control panel for the superconducting magnet power supply.

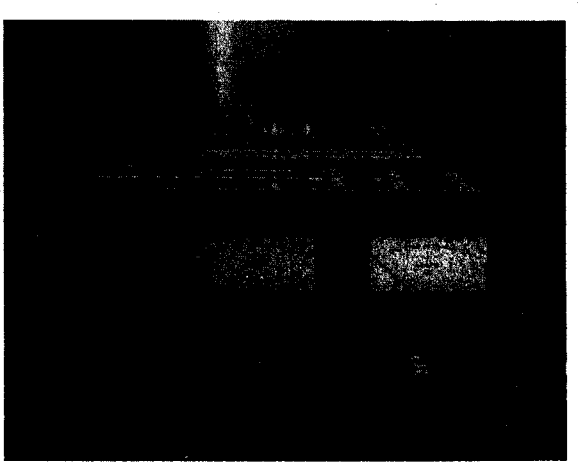

Fig. 3. The 20 kHz switching D.C. power supply.

The Control System for the 500 MeV Cyclotron

J.F.P. Marchand, B. Jeltema, and J. Jenkins

A block diagram of the control system for the new superconducting cyclotron is shown in Fig. 1. The control system is the interface between the operator and the cyclotron devices. This control system is completely computer controlled; all operator commands are processed by the computers before reading the devices and all cyclotron parameters reach the operator console through the same computer. The systems can be divided into three parts: the cyclotron subsystem (2,4), the control panel subsystem (3,5) and the supervisor subsystem (1,6,7). All devices of the cyclotron (4) are connected to a Digital Equipment Corp. PDP 11/34 processor (2) through a standard CAMAC interface system with serial highway. Processor (2) performs local processing of parameters, accepts commands and returns process parameters through the supervisory system. The console (5) is a collection of readouts, knobs, switches, etc., that allow the operator to monitor and control the cyclotron. The console is interfaced to a PDP 11/34 processor (3) through a CAMAC interface system with parallel highway. Processor (3) performs, in effect, a task inverse of processor (2); it generates commands and accepts parameters for display. All information passes through the supervisory system. Commands follow the route (5-3-6-2-4) and parameter information the route (4-2-6-3-5).

The supervisory system is built up from a PDP 11/34 processor (1), a multi-port memory (6) and peripheral equipment (7). The multi-port memory provides the interface between the various computers. The supervisory computer (1) controls the process flow and allows for program development with its peripheral devices (7). Processor (2) and (3) have no peripheral devices and are slaves of processor (1).

A departure from commonly seen computer control systems is seen at the operator console. Rather than being built up from a few standard computer terminals, the console consist of a collection of knobs, switches and readouts, each assigned to a particular function. Some rarely used devices may share controls and readouts with the help of a selector switch. This concept causes the computers to be "invisible" to the operator and has gained very good acceptance from the operators of the present 50 MeV cyclotron.

As mentioned above, the interface between computers and devices is accomplished with a standard CAMAC interface. This system consists of standard racks with plug-in modules for the particular functions. Although a wide variety of modules can be obtained commercially, it was found that, for an optimal configuration, eight different modules have to be designed and built in house. Work on these is proceeding well. Prototypes of these modules will be finished by Dec. 31, 1978.

The programming of the computers will be done mainly in a high level language. The PASCAL language is being evaluated for this purpose.

Implementation of the system described will begin Jan. 2, 1979 and it is scheduled to be operational in the fall of 1979.

The writers wish to thank R. Au, H. Blosser, W. Dumond and P. Miller for many hours of helpful discussion during the weekly computer control meetings.

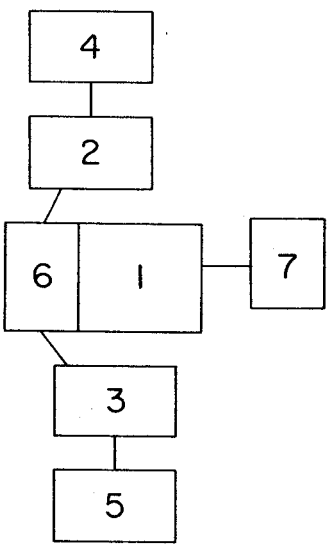

Fig. 1. Block diagram of control system:
1,2,3, Digital Equipment Corp. PDP 11/34
4 Cyclotron; 5 operators console
6 Multiport memory, 7 peripheral devices (teletype, discfile, magtape, etc.)

Studies of Stresses in the Superconducting Coil Support System

H. Blosser, D. Lawton and P. Miller

The superconducting coil for the K 500 Cyclotron is held in a position of unstable equilibrium by a set of 9 support links in tension, 3 of these links pulling up, 3 pulling down and 3 pulling radially outward at the median point. Each support link consists of a loop of epoxy and laminar glass filaments (arranged approximately as shown in the drawing on page 102 of our 1974-76 annual report). Each link is also equipped with a strain guage at its room temperature end, which allows monitoring of the forces on the superconducting coil. Magnetic forces tending to pull the coil out of position can be inferred by observing changes in the link stresses as the magnet excitation is increased.

When the magnet was initially turned on in May 1977, the pole tips had not yet been installed and the magnet gap was therefore large (36"). In this condition it was very easy to center the coil i.e., to balance the coil relative to the magnetic forces with nominal position changes of approximately 50 mils being required to produce detectible changes in the forces in the support system. Reassured by this information, the coil was turned on after the installation of the pole tips with very casual attention being paid to stresses in the support system. A memorable luncheon discussion was, in fact, being held in the vicinity of the coil as the magnet was ramping up on a particular day's measurement program when a resounding crash occurred (allegedly causing several of the luncheon attendees to demonstrate impressive antigravitational effects relative to the chairs in which they had been seated). Investigation showed that one of the radial strain gauge support bolts had broken, allowing the coil to move by approximately 1 cm under the action of the unstable magnetic force and crash into the cryostat wall. Upon inspection there was however, no damage to any of the internal systems. In a matter of a few hours, a replacement support bolt has been installed. Furthermore, the grain pattern in the broken bolt gave evidence of a previous crack and a theory of defective manufacture was immediately put forth as the explanation to the break. The ramping up of the coil was therefore resumed with the intent of continuing previously planned tests. This time, strain gauges were monitored more carefully than on the previous ramp and at approximately three-quarter excitation, an out-of-balance condition in the radial support system led to a decision to pause for a "standard" 50 mil position adjustment. This adjustment was made and approximately 30 seconds thereafter, before new strain guage readings could be recorded, the bolt break repeated. The second bolt moreover gave no evidence of unusual grain patterns associated with the magnetic flaw and in fact, showed characteristics which metalurgists judged as indicative of a pure tension break.

Fortunately the second support system failure also produced no internal damage to the coil, and was then a pleasing evidence of a great deal of ruggedness in the total system, which had not been designed with the intent that it would be subjected to such severe mechanical shocks. Also the cooling system handled the thermal pulse associated with eddy currents, etc. with almost complete smoothness, the only noticeable effect being a small rise in the helium pressure on the return side of the system.

After the second bolt break, the problem was approached with much more caution, it being obviously undesireable to subject the coil to further abuse if it could be avoided. After considerable analysis of a number of possible hypotheses, it was finally realized that the key phenomena was a very large change in the effective spring constant associated with the radial decentering force. This large change was presumably a result of the installation of the pole tips which reduced the magnet gap by an approximate factor of 10 (hill gap 2 ½"). The greatly enhanced spring constant can be seen in the data given in Fig. 1 which shows that a one mil change in the coil position has a very substantial affect on support system forces at high excitation. The one mil shift, accomplished by tightening one support bolt and loosening another, which is shown in the figure was the last in a rather lengthy series of adjustments. This particular shift led to an improved symmetry in the distribution of forces in the radial links. The force in the North link for example,in the situation designed as "initial position" in Figure 1 had ceased to decrease at 600 amps and shows a slight turning up at 650. Previous experience had shown that the upward turn could become extremely rapid under the action of the unstable spring constant and the run was therefore terminated at 650 amps and a one mil position correction was made as noted on the figure. A new ramping up of the magnet was then started and the link data showed that the force on the North link had changed to a smooth decrease. (A further adjustment might well have been considered since the force seems about to turn around at the maximum current of 700 amps--the ideal contour for the forces would be a smooth and relatively equal decrease in all three links from a not necessarily equal initial value, the decrease with current being produced by the overall expansion of the coil due to the strong radially outward magnetic force and the unequal initial positions being a result of various imperfections in the overall

construction--small radial forces transmitted by the axial links--some radial forces transmitted by various lead connections and refrigeration connections etc.)

Once the sensitivity of coil centering adjustment was realized, center of the coil was reduced to a reasonably straight forward and routine operation.

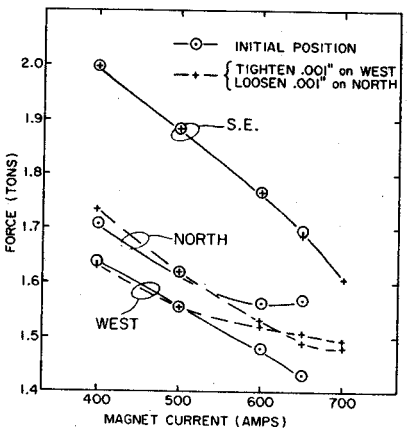

Dump Resistor Failure

M.L. Mallory

On September 19, 1977 a failure occurred in the dump resistor of the MSU superconducting cyclotron magnet. In the following paragraphs a detailed description of the consequence of this failure and the subsequent corrective action are discussed. The magnet was successfully put back into operation on October 12, 1977.

Event Leading to Failure

Fig. 1a is an electrical schematic drawing of the MSU superconducting magnet. A stainless steel dump resistor is connected in parallel with the superconducting coil at all times. The purpose of this resistor is to dissipate the energy of the superconducting coil (≈17 megajoules at 700A) in a very short time, where the normal run down time is 40 minutes. The characteristics of this resistor were designed to limit the voltage surge across the magnet coil to 200V and a current decay time of ≈3 minutes. Detailed calculations of this resistor have been reported in the 1974-76 MSU Annual Report. Initially the dump resistor had been tested by putting 700A through it from a separate power supply for ≈5 minutes, with only the boiling of water surrounding the resistor occurring. The water height above the top of the resistor was ≈6 inches. Before September 19, the superconducting coil had been dumped at lower current values, with the last dump at 600A. The only known effect was the boiling of some liquid helium in the cryostat. Between the dump at 600A and 700A, an automatic water fill system was added to the dump resistor container, with the expectation that this system would solve loss of water due to evaporation and boil off during dumps. However, the addition of this fill system resulted in the lowering of the water height above the resistor to less than one inch.

On September 19, we had completed a series of measurements at 600A and decided to run the magnet at 700A, to do measurements there and then test the consequence of dumping the magnet from 700A. At 700A, an interlock problem in the magnet power supply turned off the power supply regulator circuit and caused the magnet current to gradually decay. We decided to go ahead with the 700A dump test at this time.

Events of Failure

The dump switch was triggered and current started flowing through the dump resistor. Table I is an average of event times of five persons who were present during the entire sequence. This survey was conducted about one week after the failure. Namely, the events were first a small explosion of the dump resistor followed by arcing and flames in the magnet power supply. Next the blow-off of ≈300ℓ of liquid helium through the magnet cryostat rupture disc. Following these events were actions taken to limit the fire damage to the power supply area; isolation of the CTI 1400 refrigerator from the magnet cryostat and capping of the helium rupture disc.

Failure Sequence Hypothesis

The following hypothesis of events is proposed and is consistent with all known physical evidence. Following operation of the dump switch, current started flowing through the dump resistor, which heated the water and caused turbulence. The water turbulence then allowed the top of the dump resistor to be exposed to air and caused it to exceed the melting-point temperature. The dump resistor parted, with arcing. Fig. 1b shows the electrical circuit at that point in time. The magnetic field of the superconducting magnet was collapsing and caused the open circuit ends of the coil to raise to high voltages. Initially the current was conducted through the instrumentation leads (#26AWG) connecting to various meters, but they fused at point of coil contact. The coil voltage then increased until it broke down the insulation. The weakest insulation point appeared to correspond to the highest voltage point, and was through the warm helium gas at the top of the coil current lead. The coil at this point arced to the grounded helium can lead shield, which separates the helium system from the cryostat vacuum system. The other end of the coil was connected to the power supply, which had many (6-10) short clearance paths to ground and these paths arced to ground, completing the electrical circuit. The major energy of the coil was then dissipated in the air arcs established between the power supply and ground. The arcing of the power supply continued for about six minutes until the energy of the coil was gone. The observation of the coil temperature (≈20K) shortly after the failure indicated that little energy had been dissipated in the coil.

The arcing of the coil leads to the helium can caused it to melt (.028" thick stainless steel tubing) and allowed helium gas to enter into the vacuum jacket of the cryostat. This instantaneous heat load (estimated to be ≈20KW) on the liquid helium caused helium to boil, which then pressurized the helium can and exceeded the rupture disc pressure. The observed time for the helium plume is within a calculated factor of two for the time to boil 300ℓ of liquid helium with 20KW.

Summary of Damage Components

The magnet power supply was damaged to a very large extent. Primarily items that were designed

to carry large currents survived whereas low current items, for example the control computer and monitoring instrumentation, were destroyed. The magnet current lead and the stainless steel sheath surrounding the current lead were damaged beyond repair and were replaced. Finally ≈300ℓ of liquid helium was vented to the atmosphere.

Corrective Action

The primary corrective action was the design of a new dump resistor. The design criteria are as follows:

1. Temperature rise of 500°F (278°C), where all of the stored magnetic energy is dissipated in the two resistors and with no water cooling.
2. Resistances are calculated to match the coil inductances and give 200V across the large coil.
3. Low inductance, to prevent voltage build-up when operating the dump switch.

Table II shows the physical characteristics of the two dump resistors now built. The resistors will be operated in separate 40-gallon water tanks. The large dump resistor is stainless steel strip .024" thick by 9.2" wide, which was bent back and forth into 76 pleats, each 30" long. The full 200 ft. could not be fabricated this way in one piece, so two shorter pieces were bent and then joined with a screwed clamp and soft solder.

New Information Obtained from Failure

One of the important results of the failure has been the acquisition of new information that we would not have sought otherwise. The overpressurization of the helium can and rupture of the safety disc verified the integrity of the helium safety system. Calculations indicated that this failure was the second most severe overpressurization of the helium system, where a total quench of the magnet at full field would be the most severe. An air leak into the vacuum jacket would be expected to be about five times less severe than the helium gas leak. The voltage breakdown and damage only to the coil current lead, which are relatively easy to replace, verified the proper insulation of the coil and the correct design of the current leads for this voltage breakdown problem.

Realization that the magnet could be operated with three current leads, hence reducing the heat load on the helium system even further, was made when examining the option for replacement of the damaged coil lead. Finally, we have the sense of becoming experienced at running and operating superconducting magnets.

Table I. Event Timing

Event	Time
Dump switch opened	0
Dump resistor burned out	8 sec.
Arcing started in power supply	17.4 sec.
Firemen called	20 sec.
He rupture disc blown	23 sec.
End of helium plume	1.8 min.
Helium port corked	3.8 min.
Arcing stopped	5.6 min.
Fire out	6.0 min.
Firemen arrived	7.6 min.
New rupture disc installed	11.7 min.

Table II.

Resistor	R (ohm)	Mass (lb.)	Volume (cc)	Length	Cross Section (in^2)
Large	.30	173	9141	202.5	.23
Small	.19	110	5817	128.5	.23

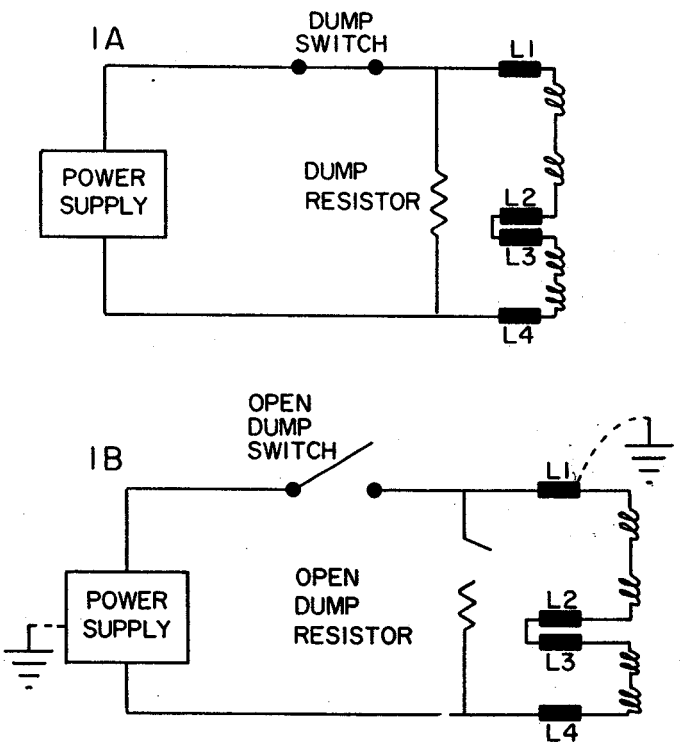

FIG. 1a. The electrical circuit of the superconducting magnet on Sept. 19. For these measurements the two sets of superconducting coils were connected in series. The dump resistor, a stainless steel wire 1/4"x1/8"x10 ft., is immersed in a 40-gallon water bucket and is connected across the coil.

FIG. 1b. The dump switch is open and the dump resistor has opened. The coil then shorted to ground at L1 and at the power supply, completing the electrical circuit.

Vacuum Calculations

M.L. Mallory

A series of vacuum calculations have been made to establish the vacuum requirements for the K=500 cyclotron. The calculations have included the charge pick-up cross section, which is important for cyclotrons, since the low energy particles traverse around the ion source and this is expected to be the largest gas load in the vacuum system. The charge stripping cross section has used the Bohr-Lienhardt equation, with the loss cross section set constant after the ion velocity has exceeded the outer electron velocity of the accelerated particle. An example of the cross section used in the calculations is shown in Fig. 1 for $^{238}U^{12+}$.

The transmission of the particles is then numerically calculated for each turn, with the assumption of constant pressure. The constant pressure assumption is experimentally correct for the cyclotron. Fig. 2 is the transmission of $^{238}U^{12+}$ in the K=500 cyclotron for various pressures and shows that greater than 90% transmission is expected for pressures of $1x10^{-7}$ Torr. A search of various beams that are expected to be accelerated on the K=500 cyclotron also gives similar results.

The calculations have been made for a series of accelerated beams on the 88" cyclotron at Berkeley and correctly predicts the measured results. In summary, the vacuum calculations require a vacuum of $\sim 1x10^{-7}$ Torr for the K=500 cyclotron.

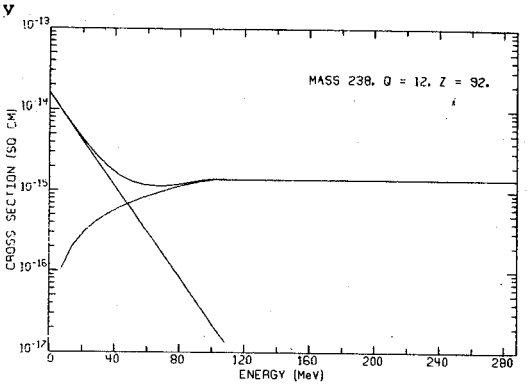

Fig. 1. The loss cross section for $^{238}U^{12+}$. as a function of energy is shown. The loss cross section has a contribution from charge pickup (dominant at low energy) and from charge stripping (dominant at high energy).

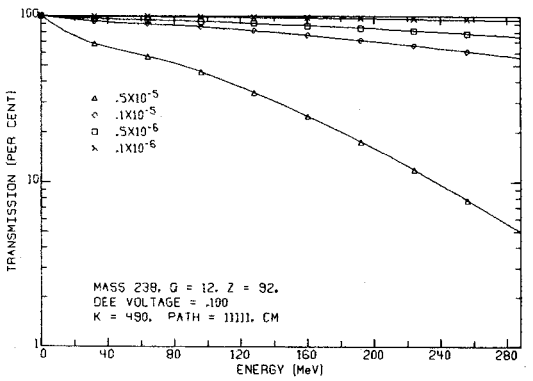

Fig. 2. The transmission of $^{238}U^{12+}$ as a function of energy for dee voltage of 100 kV. Transmission of >90% is achieved for a vacuum of $1x10^{-7}$ Torr.

Revised "Cyclone" Program for Central Region Orbit Calculations

M. Gordon, S. Motzny, and J. Bishop

The Cyclone program was developed as an aid in the design of the electrode structures in the central region of isochronous cyclotrons. The orginal version of this program was used extensively in carrying out the central region design calculations for our present K=56 MeV cyclotron. However, that program was limited to the use of two dee rf systems. We have therefore revised this program to make possible the design calculations for the K=500 MeV superconducting cyclotron which will have a three dee rf system operating in different harmonic modes.

The Cyclone program actually consists of three separate programs which have been woven together so as to make possible the calculation of an ion orbit starting from the source slit all the way out to the extraction system. Part I takes the ion from the source slit out just beyond the puller. The second part continues the orbit for a few turns until it reaches a radius of about 2.8 inch. Part III then takes the orbit out to the final radius where it enters the electrostatic deflector. These three parts differ mainly in the way they treat the rf electric field.

All three parts use the same median plane magnetic field, $B_z=-B(r,\theta)$, which is stored in a polar mesh. All such fields are produced by special separate programs, and each field is designed to meet the focusing and isochronism requirements of a specific ion with a particular final energy. The magnetic field provides an absolute reference frame for positioning the different electrodes and the resultant electric fields used in the Cyclone Program.

In Part I, the electric field in the source-puller region is derived from a potential V(x,y) which is stored in a rectangular mesh. These potentials are obtained from measurements using either conducting paper or an electrolytic tank, and such potential maps are available for several different source-puller geometries. Since the position of the source-puller must be adjusted in the design process so as to optimize the orbit centering in the main part of the cyclotron, the program provides three adjustable parameters which specify the position and orientation of the potential map. The orbit computations in this part are carried out in cartesian coordinates with time as the independent variable, but the corresponding polar variables are also furnished as part of the output.

The electric field required for Part II in the program is complicated. The three dees with the three intervening grounded electrodes all come close together in the machine center, and the exact configuration of these electrodes requires some careful study as will be seen in the following report. For a given geometry, an electrolytic tank is used to measure the potential function $V_j(x,y)$ of the j^{th} dee (j=1,2,3) with the other two dees both grounded. The three resultant potential maps are then combined in the program with appropriately phased sine waves to obtain the correct time dependent potentials used in the orbit calculations. The electrolytic tank measurements are made on a square mesh 5.6 inch on a side, with a spacing of 40 mils between points. Each map thus contains 140x140 points and requires about seven hours to measure.

In Part III of the program the electric field is represented as a delta function in each of the six gap crossings occurring in one revolution. The resultant energy gain also includes a transit time factor which takes account of the finite width of the electric gap. In addition, the ion orbit receives a radial impulse arising from the spiral curve of the dee gap line. This semi-analytic representation of the electric field effects allows this part of the program to run very fast compared with Part II. Using a table of stored equilibrium orbits, the program will print out once per sector the displacement of the accelerated orbit, thereby determining the centering error for this orbit.

This Part III of the program exists separately as one version of the "spiral gap" code. This code can run backwards as well as forwards, and backward runs starting from centered orbits provide valuable information for obtaining a preliminary electrode design which is then used to obtain electrolytic tank measurements. These measurements together with Cyclone orbit calculations can then be used to confirm the design or to indicate necessary revisions. Through such an iteration process, a final optimized design is obtained for the central region electrode structures.